



DURHAM UNIVERSITY

MPhys PHYSICS WITH ASTRONOMY FINAL YEAR PROJECT

Galaxy formation over the last 8 billion years: How do the first spiral disks form and evolve?

Alexander Hill

supervised by

Dr. A M SWINBANK

April 27, 2016

Abstract

We present spatially resolved spectroscopy of a sample of 102 H α selected galaxies at $z = 0.78 - 1.04$, of which 72 are found to have an S/N ratio greater than 7 and are further investigated. We calculate a SFR of $5 - 29 \text{M}_\odot \text{yr}^{-1}$, which is representative of the general high-redshift star forming population. Using spatially resolved H α dynamical observations, of resolution $\sim 1.5 \text{kpc}$, we find that of the 72 analysed galaxies, 60 have velocity fields and gradients consistent with the galaxies having their ionised gas in large, rotating disks. We inclination-correct their derived one dimensional rotation curves and fit a simple arctan function in order to determine whether the rotation curve turns over. We use the rotational velocities and the maximum observed radii to derive dynamical masses, and assuming that dark matter constitutes 70% of the total mass we infer $f_{\text{gas}} = 0.2 \pm 0.1$, consistent with the high gas fractions observed in star forming galaxies at high redshift. We use the spatial variation of NII/H α and the $N2$ index to calculate an average $\Delta \log(\text{O}/\text{H})/\Delta R = -0.026 \pm 0.019 \text{ dex kpc}^{-1}$, which shows that relative chemical abundances in galaxies at this redshift decrease with galactocentric radius. This is consistent with the predictions of the GIMIC simulation for the metallicity gradients of galaxies at high redshift. We calculate the stellar component of the angular momentum of our star forming galaxies and find that they occupy the same parameter space as local spirals. We calculate the spin parameter λ_R , and find a median value of 0.55 ± 0.04 . We also find that it does not strongly correlate with the stellar mass.

Contents

1	Introduction	2
2	Samples, Observations and Data Reduction	4
2.1	<i>KMOS IFU Observations and Data Cube Construction</i>	4
2.2	<i>Stellar Mass, Dust Attenuation and Redshift</i>	5
3	Analysis	7
3.1	<i>Integrated Galaxy Properties</i>	10
3.2	<i>Flux, Star Formation Rate and Metallicity</i>	10
3.2.1	<i>Star Formation Rate</i>	10
3.2.2	<i>Metallicity</i>	13
3.3	<i>Internal Dynamical Observations</i>	15
4	Results and Discussion	16
4.1	<i>Spatially Resolved Metallicity Gradients</i>	16
4.2	<i>Rotational Velocity and Velocity Dispersion</i>	18
4.2.1	<i>Angular Momentum</i>	23
4.2.2	<i>Spin</i>	25
4.2.3	<i>Dynamical Mass</i>	25
5	Conclusion	27
6	References	29
7	Appendix	30

1 Introduction

Constraining the formation and evolution of galaxies with redshift is one of the key areas of modern astrophysics. The current consensus is that the star formation rate density of the universe peaked 3.5 Gyr after the big bang and declined by an order of magnitude below $z \sim 1$ (e.g. Madau & Dickinson 2014; Shapley 2011; van de Voort 2011; Genzel 2010). The majority of stars present in the most massive galaxies today ($> 10^{11} M_{\odot}$) were formed during this period (Sobral et al. 2012). Galaxies at the epoch appear to be gas rich ($f_{gas} = 20\text{--}80$ per cent) and highly turbulent (Daddi et al. 2010; Tacconi et al. 2010). Numerical simulations suggest that the high rates of star formation are continuously fuelled by the accretion neutral HII gas (Bournard & Elmegreen 2009; Dekel et al. 2009; van de Voort et al. 2011). The dominant sources of this gas appear to be cold streams from the intergalactic medium (IGM), accretion from the halo and minor mergers. This suggests that the star formation process is driven by the internal dynamics of galaxies (Kereš et al. 2005). The challenge, therefore, is to correlate the observational properties of the star forming galaxies with the real physical parameters and how they vary with redshift. The main goal of this project is to measure the dynamics of galaxies at the time of peak formation and analyse the interaction between the gas and stellar populations within the interstellar medium, in order to provide constraints for models that aim to describe the evolution of these heavily star forming galaxies into the spirals we see today.

One way in which we can trace star formation is through the analysis of the $H\alpha$ emission line, which arises from the recombination of hydrogen gas after ionisation by UV photons emitted by massive, short lived stars. The brief (cosmologically speaking) lives of these massive stars means that their very presence is synonymous with ongoing

star formation. Analysing the spatial variation of $H\alpha$ emission lines across the disks of star forming galaxies therefore gives us an indication of the varying properties of star forming regions across a galaxy. An additional advantage of observing a galaxy in $H\alpha$ is that for $z \sim 1$ galaxies, the light we receive has been redshifted into the infrared and can therefore penetrate the atmosphere and be observed by ground based telescopes, such as the VLT¹. Infrared sampling has the additional advantage of reducing bias in galaxy sampling; starburst galaxies (galaxies undergoing a brief period of rapid star formation following a sudden increase in the gas supply) are often surrounded by dust following mergers, meaning that they are invisible in many parts of the spectrum. These galaxies shine brightly in the IR and so are observable in $H\alpha$. Sampling in $H\alpha$ therefore gives us a more representative set of galaxies to analyse than in the optical, for instance.

It has been shown that the majority of star forming galaxies at $z \sim 1$ have their ionised, highly turbulent gas in large rotating disks. The fractions of gas in these disks are significantly larger than is observed in local spirals (Daddi et al. 2010; Tacconi et al. 2010). Connecting the dynamics of star forming galaxies at high and low redshifts by evolutionary models provides insight into the relationship between star formation and gas content.

The interplay between gas accretion and star formation also has consequences on the chemical enrichment of the ISM. The once pristine ISM is enriched as massive stars go supernova and disperse heavy elements. At the same time, gas accretion provides a supply of HII to the edges of the galaxy. The spatial variation of chemical abundances across a galaxy gives an insight into the history of both its star formation and gas accretion (Solway et al. 2012). If the dominant mode of gas accretion is

¹eso.org/sci/facilities/paranal/telescopes/ut.html

cold streams from the IGM, there should be an observable strong negative metallicity gradient, caused by gas being deposited at large radii (10-20kpc) and star formation being concentrated in the bulge (Dekel et al. 2009). The gradient will grow shallower at lower redshift as the gas accretion becomes less efficient and the gas is dispersed around the disk (Swinbank et al. 2012).

Investigation into the internal properties of galaxies has opened up in recent decades, with the advent of integral field spectroscopy, which marries spectroscopy and imaging to allow the analysis of a galaxy over multiple wavelengths, and integral field units (IFUs) which employ bundles of fibres to spatially resolve the light being emitted from a galaxy, allowing the creation of an emission spectrum for each pixel. The spectral features of each emission spectrum give us an insight into the physical conditions at each pixel.

We will attempt to prove that the majority of the star forming galaxies selected in our sample are indeed rotating disks by comparing the Doppler shifted H α emission lines of each pixel with that of the galactic centre, thereby creating a two dimensional velocity field. From this we shall derive a one-dimensional rotation curve, from which we shall derive the dynamical mass of each galaxy and compare it with the stellar mass. This shall give us an indication into the amount of gas that was available for the fuelling of star formation at this peak redshift. We shall also calculate the ratio v/σ , where σ is the median velocity dispersion, which measures the rotational-thermal support. High-redshift galaxies tend to have high velocity dispersions given their rotational velocities (Swinbank et al 2012); we shall attempt to show that our results are in agreement with previous results in this case. High dispersion areas indicate the presence of a thick band of gas along the line of sight. We therefore expect dispersion to be centrally peaked at bulge, although isolated high disper-

sion areas in the extremities of the disk can provide evidence for 'clumps', massive ($\sim 10^{8-9} M_\odot$) star forming regions formed by the fragmentation of dynamically unstable gas (Elmegreen et al. 2007). These clumps play a key role in the build-up of stellar mass in the disk and the bulge, and therefore in the evolution of galaxies.

We shall measure the metallicity of the galaxies in our sample by using of the flux ratio [NII]/H α and the $N2$ index (Pettini and Pagel 2004), which relates this to the more commonly used metallicity indicator $12 + \log(\text{O/H})$. The advantage of measuring metallicity by using an oxygen tracer is that its relative abundance is greater than all other elements heavier than hydrogen and that it exists almost entirely in the gas phase (Snow et al. 1996).

Two of the more basic properties of galaxies that one can measure through observations are their angular momentum and mass. Restricting these to the stellar content of galaxies, we find that j_* and M_* , the specific angular momentum and stellar mass respectively, are fundamentally linked. Their relationship is so tightly defined that we find different morphologies of galaxies occupy different areas in $j_* - M_*$ parameter space (Romanowsky & Fall 2012). This provides a physics based alternative to the traditional Hubble sequence in galaxy classification. Comparing $j_* - M_*$ for star forming regions at $z \sim 1$ to results for local, more clearly categorised galaxies can give an indication into the nature of the galaxy population at this peak epoch. Here we shall use dynamical observations to do exactly that. Galaxies at high redshift are found to have a higher j_* than their low redshift counterparts, so for these disks to be connected by an evolutionary pathway there must take place at least one process that causes a gain in angular momentum. The relationship between j_* and M_* therefore provides important constraints on evolutionary models.

We shall also calculate the spin parame-

ter, λ_R , for our galaxies. λ_R has been suggested as a proxy for specific angular momentum (Emsellem et al. 2011), so we shall here compare its relationship with the stellar population of our sample via the star formation rate (SFR), specific star formation rate (SSFR) and stellar mass.

In this paper we present adaptive optics assisted integral field spectroscopy with KMOS (Sharples et al. 2013; Davies et al. 2013) of 102 star forming galaxies selected from the HiZELS (Sobral et al. 2012) and COSMOS (Koekemoer et al. 2007) surveys over the redshift range $z = 0.78 - 1.04$. We use H α measurements to investigate the dynamical properties of the galaxies and the star formation and chemical enrichment within their ISM. We use a cosmology with $\Omega_\Lambda = 0.70$, $\Omega_m = 0.30$ and $H_0 = 70$ kms $^{-1}$ Mpc $^{-1}$. In this cosmology, at the median redshift of our survey, $z = 0.86$, a spatial resolution of 0.2 arcsec corresponds to a physical size of 1.54 kpc. For all stellar masses and star formation rates, we use a Salpeter (1955) Initial Mass Function.

2 Samples, Observations and Data Reduction

To analyse the dynamics of galaxies at the time of peak star formation, $z \sim 1$, we selected target galaxies from the HiZELS and COSMOS surveys to be observed by the Integral Field Units (IFUs) K-band Multi Object Spectrograph (KMOS) on the VLT. These instruments combine imaging and spectroscopy to perform Integral Field Spectroscopy, allowing for the observation of a galaxy's spectral energy distribution (SED) on a pixel-by-pixel basis. From the initial sample of galaxies observed by KMOS, we worked with a subset of 102 galaxies which had a median stellar mass of $1.1 \times 10^{10} M_\odot$ and were representative of the group, as shown in Fig. 1. Of the 102 galaxies, evidence for H α emission was found in 72, indicating that these are star

forming, whereas the others are undergoing a period of dormancy (quiescence).

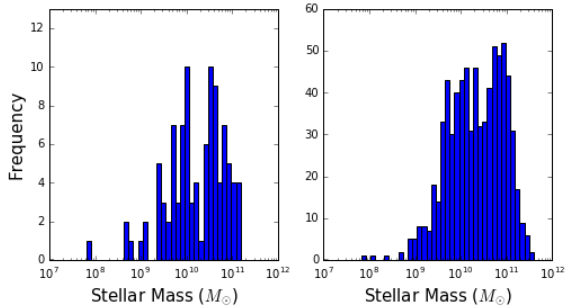


Figure 1: (Left) A histogram showing the range of stellar masses in the galaxies analysed in this report. (Right) A histogram showing the range of stellar masses in the total galaxy population available to us. The bulk of the galaxies in both cases have a stellar mass between $10^9 - 10^{11}$. In terms of stellar mass, our sample appears to be representative of the total population observed by KMOS

2.1 *KMOS IFU Observations and Data Cube Construction*

Observations were made using the KMOS multi-object IFU system on the VLT, which employs 24 IFUs across a patrol field of 7.2 arcmin in diameter. The instrument used 24 adjustable arms that position pickoff mirrors at locations specified by the user. The subfields selected are then fed into 24 separate IFUs which slice each subfield into a 14-by-14 equipartitioned grid, with 14 spatial pixels along each slice. The light from this grid is then dispersed by three cryogenic grating spectrometers which generate a spectra for each individual pixel for each of the 24 independent subfields.

Each IFU has a square field of view of 2.8×2.8 arcsec, leading to a spatial resolution of 0.2''. In the measurement of each pixel's SED, we operated in the K-band where KMOS has a wavelength coverage of 1.934 - 2.460 μm and a spectral resolving power of $R = \lambda/\Delta\lambda \sim 4400$.

The main reason we used KMOS was its ability to perform Integral Field Spectroscopy (IFS) in the near-infrared. The H α and NII lines, with rest wavelengths of

6562.8Å and 6583Å, emitted by galaxies at $z \sim 1$ are redshifted into the near-infrared by the time they reach the Earth. This allows the light to penetrate our atmosphere relatively unimpeded and be observed by our telescopes. Operating KMOS in the K-band and performing IFS, we obtained what is known as a 'data cube'. Of this three-dimensional array, the x and y- axes of these cubes are spatial, whereas the z-axis represents wavelength (see Fig. 22 in the Appendix). In practice, this means that we can collapse the cube to a certain z-coordinate and view how brightly the galaxy shines at a certain wavelength (see Fig. 2). We can also fix a group of spatial pixels and record how the flux changes with wavelength, constructing an emission spectra for that range (see Fig. 3). The link between these two and how we generated each of them is explained in more detail in Fig. 4. We incorporated a 3σ cut-off for flux values for each wavelength slice, removing any pixel values associated with cosmic rays.

The beauty of an IFU is that we can obtain an emission spectrum for each of the pixels in the 14×14 grid partitioning each galaxy. The variation of features in each spectrum gives astronomers an indication of how the physical properties of galaxies vary across their bodies. We further explain this in Section 3.3. In the next section we shall investigate the integrated properties of our sample of galaxies.

2.2 Stellar Mass, Dust Attenuation and Redshift

The stellar masses of the galaxies in this report were calculated via a combination of observations and numerical simulations. The observed broad-band emission spectrum of each galaxy can be interpreted in terms of its integrated stellar, dust and metal content and its past star formation periods. The process of creating a synthetic SED based on these properties was first attempted by Tinsley (1968). These simu-

lations attempt to match actual observations of galaxies and determine the intrinsic physical properties of galaxies based on their observed properties. As these techniques have grown more sophisticated, they have played a greater part in the determination of galactic properties. The stellar population can be described at any time by use of an Initial Mass Function (IMF) and a Star Formation History (SFH). The IMF is a function that describes the initial distribution of masses of stars following the collapse of a gas cloud. The function that describes this distribution was described first by Salpeter (1955) as a power law of the form

$$\Phi(\log m) = dN/d\log m \propto m^{-\Gamma}, \quad (1)$$

where m is the stellar mass and N is some logarithmic mass range $\log m + d\log m$. 'Salpeter-like IMF's' are those which have a 'Salpeter index', Γ , of approximately 1.35. This means that for a given star forming region, high mass stars are much less likely to form than lower mass stars. The potential variability of the form of the IMF with redshift is debated to this day, and is summarised in the excellent review '*A Universal Stellar Initial Mass Function? A Critical Look at Variations*' by Nate Bastian et al. (2010). If the IMF did indeed vary at high redshifts or in extreme locations, it would have great effects on our models for galaxy evolution, which presently assume a power-law IMF of Salpeter index ($\Gamma = 1.35$) above a few solar masses, and a shallower power of ($\Gamma \approx 0-0.25$) between a few tenths and a few solar masses. While the shape and universality of the IMF at the stellar-substellar boundary is still an area of active research and uncertainties remain large, most observations are consistent with an IMF that declines ($\Gamma < -0.5$) well below the hydrogen burning limit (Bastian 2010; Bromm 2001). In this report we shall assume that the IMF is invariant, with $\Gamma = 1.35$. The IMF is a very useful tool for astronomers which,

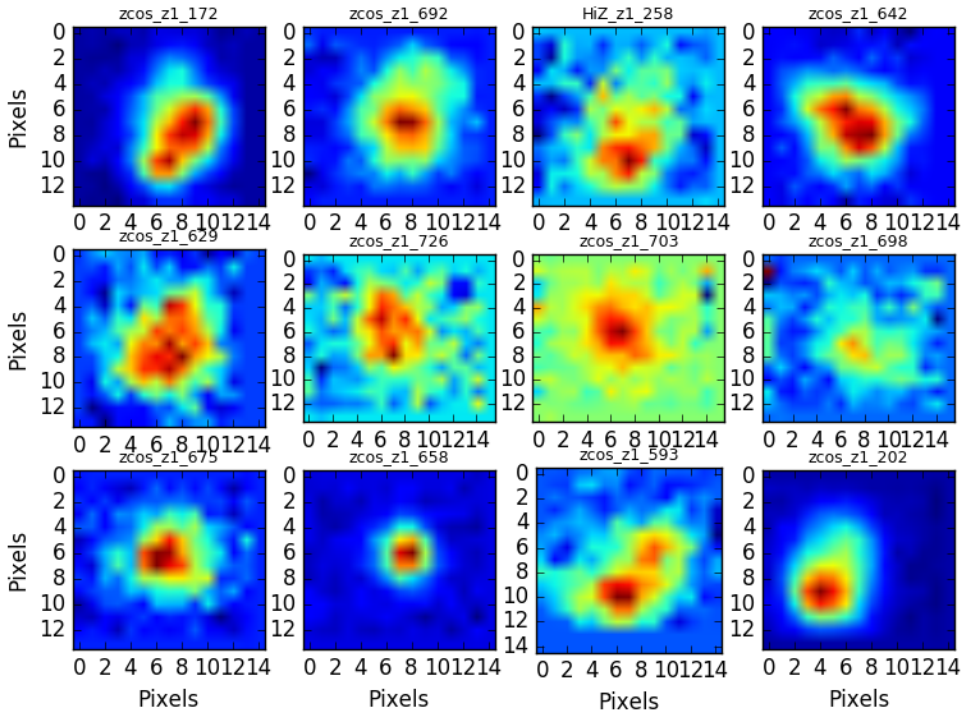


Figure 2: Narrow band images of H α emission taking place in a sample of the galaxies we worked with. These galaxies were first observed in the COSMOS and HiZELS survey and are identified by their IDs in these surveys. The images are created by collapsing the data cubes obtained from integral field spectroscopy performed by KMOS. We cut the cube down to a 14×14 grid in the $x - y$ plane and 11 neighbouring pixels in the axis corresponding to wavelength. This is centred in each case about the assumed redshifted observed H α wavelength. We sum along the z axis to create a High Dynamic Range image (HDR). We can see that all the galaxies on display shine brightly in terms of H α emission and hence are currently undergoing star formation. The HDR images have been 'smoothed' using an interpolation technique to make the structure of the H α emitting regions more easily discernible. The median H α flux for this sample is $1.4 \pm 4 \times 10^{-16}$ erg s $^{-1}$ cm $^{-2}$.

among other things, allows us to calculate an entire stellar population despite only observing a subset of them. We shall discuss this in greater detail in Section 3.

Combining a specific stellar IMF with a given SFH, we can follow the evolution of the stellar population as the clock runs forward. Each star in the population has an emission spectrum, which can be characterised by their position on the Hertzsprung-Russell diagram. For an arbitrary stellar population, the integrated SED of every star is computed by the individual contributions of each star.

Things get complicated when one attempts to include the effects of dust in the model. Interstellar dust absorbs photons produced by the stellar population,

resulting in absorption lines in the SED, and then reemits photons of a variety of wavelengths as the particles de-excite. This is hard to model and the uncertainties involved are large, though many theoretical models (Charlot & Fall 2000) and empirical parameterisations (Calzetti et al. 2000) take describe SEDs in terms of stellar content and dust content. The evolution of stellar populations can further be modelled by including the rate of Type I and Type II supernovae. It has been suggested (Shapley 2011) that the most widely used models are those of Bruzual & Charlot (2003).

A multitude of simulations with a variety of parameters are conducted. The resulting theoretical SED that closest matches observations is stored, and we infer vari-

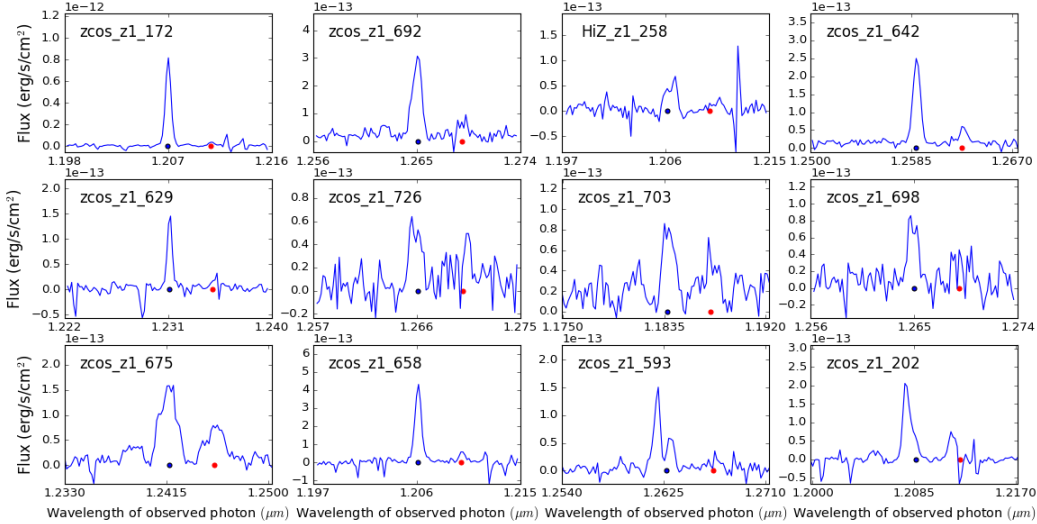


Figure 3: Spatially integrated, one-dimensional emission spectra centred on the redshifted H α for a sample of the galaxies investigated in this report. These galaxies are the same as the ones whose narrow band images are displayed in Fig. 2. The IDs of the galaxies were constructed from the surveys in which they were first identified (HiZELS and COSMOS). In each case, we note the predicted location of the H α and [NII] λ 6583 emission lines with a blue and red dot respectively. In all cases we see evidence for H α emission and some evidence for NII emission, though on a much lower scale, suggesting low metallicity in these galaxies.

ous physical properties. The stellar mass of the galaxy is calculated by finding the total mass of the stellar population in the matching synthetic model. The dust attenuation factor and redshift of each galaxy are similarly inferred by matching the properties of synthetic properties to observations.

The dust attenuation factor, A_v , describes how the intrinsic H α flux differs from the observed flux as $I\text{H}\alpha_{\text{int}} = I\text{H}\alpha_{\text{obs}}e^{A_v/2.5}$. Interstellar dust has the additional effect of introducing selection bias into our sampling. Galaxies which are enshrouded in dust, a known population often with high SFR (Hammer et al. 2005), may have so much of the optical light absorbed that they are not detected in surveys. HiZELS and COSMOS attempt to mitigate this bias by conducting observations in the near IR (NIR) and mid-IR. As well as absorbing UV and optical light from stars, dust also re-emits in the IR and submillimetre wavelengths. With this knowledge, we can identify galaxies with a high dust content and attempt to convert the observed fluxes to intrinsic fluxes. The problem with

this is that there is an unknown effect of dust heating caused by elderly stellar populations (Bell 2005).

The dust covered galaxies with high SFRs may be considered to be experiencing a brief period of SF caused by mergers or gas-infall. The limited amount of gas made available in these occurrences means that for most of their lifetimes the galaxies are on the main-sequence of galaxy evolution with much lower specific star formation rates (SSFR). They are in effect a brief interlude in the normal process of galaxy formation. Due to the difficulty in detecting these galaxies, it may be that the galaxies in our sample are towards the lower end of the star forming population. Indeed of the 102 originally sampled, 30 showed no signs of H α emission and may therefore be considered to be quiescent.

3 Analysis

Upon obtaining H α centred emission spectra for each of the 102 galaxies, we attempted to fit the data with a model Gaussian function in order to parameterise our

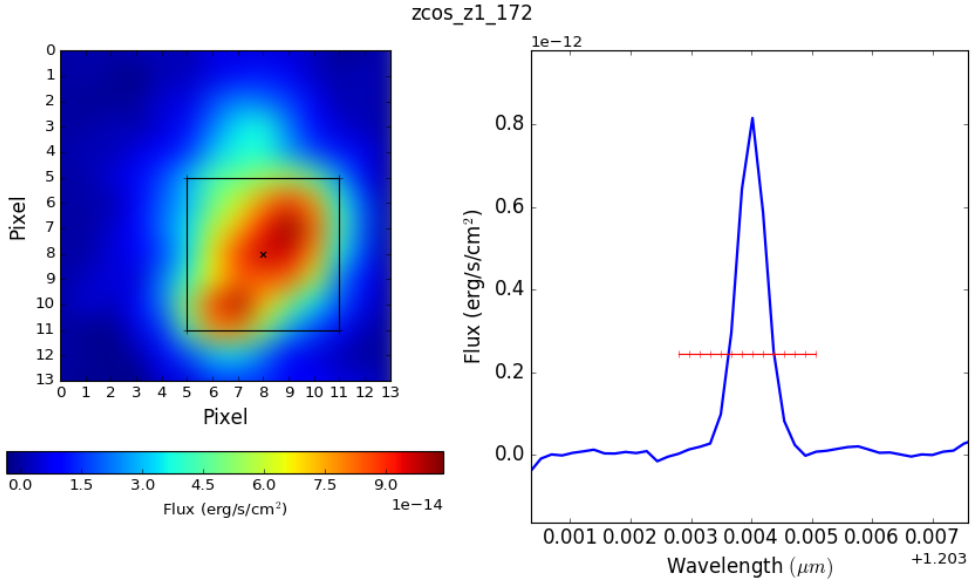


Figure 4: An explanation of how the data from KMOS was interpreted for each galaxy to produce (**Left**) a narrow band image of the H α emission of galaxy zcos_z1_642 and (**Right**) the one dimensional emission spectra of the same galaxy centred on the redshifted H α line. The image was created by collapsing the KMOS generated data cube along the z (wavelength) axis and summing over the region indicated in the emission spectra by the dashed red line. Summing the slices over this range ensures that we are observing the full H α flux from the galaxy, which can be seen in the emission spectra as the summing region clearly encloses the entirety of the prominent H α emission line. We know that this is the H α line as it is centred on the location we would expect given the galaxy's redshift, which is represented by the black cross at $1.259\mu\text{m}$. The emission spectra was generated by a process which involved first finding an approximation of the galaxy's centre, which was achieved by finding the pixel coordinate in the 'smoothed' narrowband image with the greatest flux value. The smoothing process involves replacing each pixel value with the median value of the pixels surrounding it, which shows us which area of the galaxy is emitting the most flux on average and is thus a fair approximation of the galactic centre. Upon finding the galactic centre, marked with a black cross, we constructed a grid of pixels around it which roughly encloses the main body of H α emission in the galaxy. We then recorded how the flux total enclosed in the grid varied with wavelength. This is the integrated emission spectra for the galaxy about H α .

data. This function takes the form

$$f(n) = b + \frac{I_{H\alpha}}{\sqrt{2\pi}\sigma} \exp\left[\frac{(x - \lambda_{H\alpha})^2}{2\sigma^2}\right] + \frac{I_{NII}}{\sqrt{2\pi}\sigma} \exp\left[\frac{(x - \lambda_{NII})^2}{2\sigma^2}\right] \quad (2)$$

where b is the background intensity, I is the intensity (flux), λ is the wavelength of the emitted photon and σ is the velocity dispersion. $\frac{I_{H\alpha}}{\sqrt{2\pi}\sigma}$ ensures that the flux we obtain from our Gaussian fitting is the integrated flux, which in terms of the emission spectra is the area underneath the H α emission line. We did this as we assumed the H α emitting regions to be in a gas phase and for the main sources of broadening to be from the Doppler effect. The velocity of atoms or molecules present

in the gas along the line of sight follow a Maxwell distribution, meaning that the effect is dependent only on temperature, leading to a Gaussian distribution (Hillas 1996). We optimised the parameters for the Gaussian function to our emission spectra using the python function `scipy.optimize.curve_fit`. We took into account sky emission, hereafter referred to as the sky background, by overlaying our emission spectra with the sky background. In the least-squares minimisation function used by the optimisation function, `np.sum(((f(xdata,*popt)-ydata)/sigma)**2)` (where $f(xdata, *popt)$ is the Gaussian function with parameters to be optimised $*popt$), the sky background was taken to be the uncertainty in the y-data, σ . Further detail into the

optimisation can be found at docs.scipy.org/doc/scipy/reference/generated/scipy.optimize.curve_fit.html. Upon obtaining the optimised parameters we entered them into our Gaussian function and compared this model with our observed data. An example of this can be seen in Fig. 5.

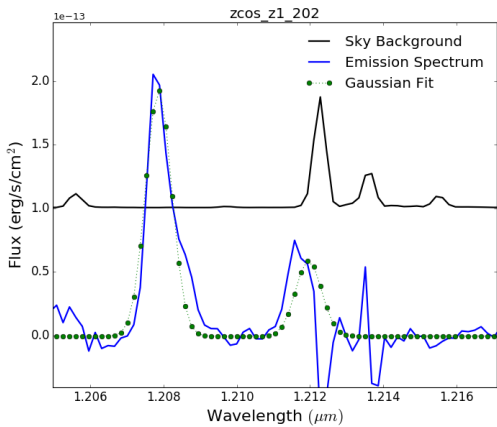


Figure 5: The integrated one dimensional emission spectrum for galaxy zcos_z1_202. Overlaid in black is the normalised sky background emission spectra and has been shifted up the plot so the two sets of data are more easily discernible. We can see here that the sky background emission lines correspond to points of increased noise in our galaxy emission spectra. The data points of the sky background are taken to be the uncertainty in the observed flux when using a least squares minimisation function as part of the optimisation of a Gaussian fit to the emission spectra. The optimised parameters and the relevant wavelength range are entered back into our Gaussian function and form our model, shown here in green. In this case our model appears to fit the raw data very well for the H α and NII emission lines.

Upon fitting a Gaussian function to the integrated emission spectra of all 102 galaxies, we tested the goodness of fit of our model against that of a straight line model. We first found the value of χ^2 , which is a dimensionless quantity that describes the ‘goodness’ of a model fitting to measured data. This was calculated by

$$\chi^2 = \sum \frac{(y_i - y(x_i))^2}{\sigma_i^2}, \quad (3)$$

with y_i being the observed data point, $y(x_i)$ being the model value and σ being the ‘noise’. The noise was taken as being the

standard deviation of background noise in the continuum of the emission spectra. To find this we isolated a ‘featureless’ part of the spectrum, that is a small wavelength range devoid of any major known emission lines. We then calculated the standard deviation of the fluxes, incorporating a rough clipping of any large features that appeared to correspond to sky background emission lines.

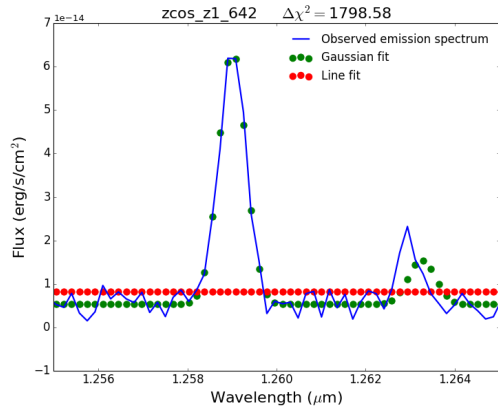


Figure 6: A comparison of a Gaussian and straight line fit to the integrated emission spectrum of zcos_z1_642. The Gaussian fits the data better than the straight line, leading to a $\Delta\chi^2$ value of ~ 1800 and a SNR of 42.4. This confirms that this galaxy is a strong H α emitter and should be further analysed.

Taking the χ^2 value for the Gaussian and straight line fits, we calculated $\Delta\chi^2 = \chi_L^2 - \chi_G^2$, which gives us the signal to noise ratio (SNR). The theory behind this is that the Gaussian model will fit to the emission lines and the continuum whereas the straight-line will fit to the background alone. For a galaxy with prominent H α and NII emission lines, the Gaussian function will fit the data much better than the line model which will lead to a large $\delta\chi^2$ value. To ensure that we were working with the ‘cleanest’ data, we removed any galaxies which had $\delta\chi^2 < 49$ for a Gaussian fit to the integrated emission spectrum. An example goodness of fit test can be seen in Fig. 6. This corresponds to a signal to noise ratio, S/N, of 7. From this we were left with 72 galaxies which were confirmed emitters of H α and therefore undergoing star for-

mation. We shall analyse these in greater detail in the rest of the report.

3.1 Integrated Galaxy Properties

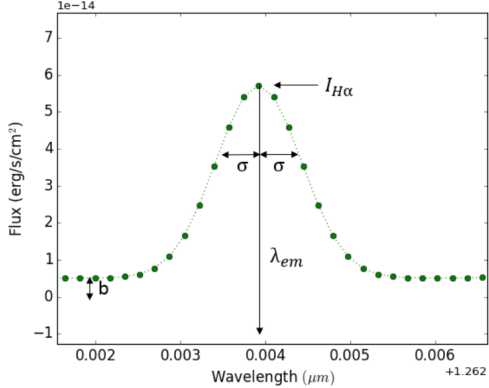


Figure 7: Function created by fitting a Gaussian curve to the H α centred integrated emission spectrum of a galaxy. This curve is parameterised by the height of the curve’s peak ($I_{H\alpha}$), the position of the peak’s centre ($\lambda_{H\alpha}$), the standard deviation of the peak (σ) and the background level (b). We use the optimised values of these parameters to infer many physical properties of the galaxy.

The Gaussian fitting allows us to parameterise data and infer physical properties of our galaxies, but how exactly do we go about this? While in Eq. 2 we use a superposition of two Gaussian functions to model both H α and NII emission, in Fig. 7 we only display the part of Eq. 2 relevant to the H α emission line for clarity. This Gaussian has four parameters: $I_{H\alpha}$, $\lambda_{H\alpha}$, σ and b . How we interpret these values to calculate the integrated physical properties are detailed below.

3.2 Flux, Star Formation Rate and Metallicity

3.2.1 Star Formation Rate

The Star Formation Rate Density (SFR- ρ) gives us an indication of how exciting the universe is. One of the most famous plots in cosmology is the Madau plot (Fig. 8), which displays how the SFR- ρ of the universe has changed with redshift.

Our first objective in the analysis of these $z \sim 1$ galaxies was to see whether

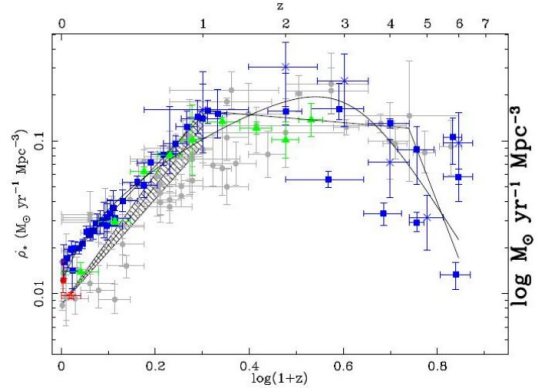


Figure 8: The star formation rate density (SFR- ρ) as a function of cosmic time (redshift), with $z = 0$ being the present day. The SFR rises exponentially to peak at $z \sim 2$ and then decreased sharply up to the present day (Shapley 2011). One of the main focuses of research in cosmology is the investigation of the evolution of galaxies, with a particular focus on the dynamics of galaxies at $z \sim 1 - 2$ and how they fit into a wider context of galaxies at all redshifts.

their inferred SFRs are indeed larger than those of local galaxies and whether they match previous studies into galaxies at similar redshifts. We calculated the SFR by using the H α emission flux of each galaxy as a proxy.

This part of the spectrum traces young stellar populations, other diagnostic methods include the rest-frame UV and IR luminosities of star forming regions. These diagnostic methods are sensitive to only the presence of short lived, massive stars. Given the short lifetimes of these stars, it is reasonable to assume that their presence indicates that star formation is in fact occurring. The estimation of the total SFR requires the assumption of a particular form of the IMF, which is then used to extrapolate the known young, hot star mass down to the low stellar masses that dominate the integrated stellar mass (Shapley 2011; Bromm 2001).

The hot, massive and short lived stars with $M > 16M_\odot$ emit photons which ionize nearby interstellar gas, the subsequent emission from the recombining hydrogen gas serves as a substitution for the rate of production of ionizing photons, which then leads to the formation rate of mas-

sive stars. As the ionising flux is dominated by the emission from the stars with more than ten solar masses, it provides an estimate for the instantaneous rate of star formation. With ground-based observations, H α emission lines have been measured for star forming galaxies up to $z \approx 2.6$ (beyond which point the atmosphere is opaque to the extremely redshifted radiation) and used to estimate star formation rates (Erb et al. 2006; Förster-Schreiber et al. 2009).

We first needed to calculate the intrinsic bolometric luminosity of the H α emission, which was done by assuming that the H α is emitted equally in all directions and integrating over the luminosity distance. This equation takes the form

$$L = 4\pi S D_L^2, \quad (4)$$

where L is the bolometric luminosity, S is the observed flux and D_L is the luminosity distance. We calculated the D_L as described by Hogg (2000), which we will summarise here.

In order to find the luminosity of a galaxy from the flux, the luminosity distance must first be calculated as a function of redshift and the dimensionless present day density parameters of the universe. Ω_k is the spatial curvature density, Ω_λ is the vacuum density and Ω_M is the matter density. These values are related as $\Omega_\lambda + \Omega_M + \Omega_k = 1$.

We define the Hubble distance as the Hubble time multiplied by the speed of light

$$D_H = \frac{c}{H_o}. \quad (5)$$

We also define δD_C , the infinitesimal comoving distance between two objects, as the proper distance divided by the scale factor. D_c is the total comoving line of sight distance, which is calculated by integrating all the infinitesimal comoving distance contributions between nearby events along the radial ray from the observer at $z = 0$ to the distant object.

We define $E(z)$ as

$$E(z) = \sqrt{\Omega_M(1+z)^3 + \Omega_k(1+z)^2 + \Omega_\lambda} \quad (6)$$

where $H(z) = H_o E(z)$. As $dz = da, dz/E(z)$ is proportional to the time of flight of a photon across the redshift interval dz divided by the scale factor at that time. The speed of light is constant, so this is the proper distance divided by the scale factor. We now have $D_C = D_H \int_0^z \frac{dz'}{E(z')}$.

We define the transverse commoving distance as D_M , where $D_M \delta\theta$ is the distance between two objects at the same redshift separated by some angle $\delta\theta$. D_M is related to D_C by:

$$D_M = \begin{cases} D_H \frac{1}{\sqrt{\Omega_k}} \sinh[\sqrt{\Omega_k} D_C / D_H] & \text{for } \Omega_k > 0 \\ D_C & \text{for } \Omega_k = 0 \\ D_H \frac{1}{\sqrt{|\Omega_k|}} \sin[\sqrt{|\Omega_k|} D_C / D_H] & \text{for } \Omega_k < 0 \end{cases} \quad (7)$$

The luminosity distance is related to the transverse comoving distance by $D_L = (1+z)D_M$.

We converted the bolometric luminosity L to total SFR by use of a conversion factor

$$\text{SFR}(M_\odot \text{yr}^{-1}) = 7.9 \times 10^{-42} L(H\alpha)(\text{erg}\cdot\text{s}^{-1}). \quad (8)$$

This conversion factor was calculated by Kennicutt et al. (1998), who made use of a Salpeter IMF to infer the total stellar population from knowledge of only the highest mass stars. If the IMF does indeed vary with metallicity and location, as may be the case at extremely high redshift, then it is very likely that the inferred SFR, stellar mass and density would be systematically in error, which would in turn lead to systematic errors in our models of galaxy formation and evolution. The next generation of telescopes, such as the ELT, are set to make high-redshift galaxies easier to study in detail than ever before. As large variations in the IMF have seemingly been ruled out, detailed analysis of the Universe

at redshift $z \sim 2$ will allow us to better constrain subtle variations in the IMF with initial conditions (size of cloud, metallicity etc.). Spatially resolved rest-frame UV spectroscopy of star forming regions in these early galaxies will be within our capabilities, allowing comparison with local templates. In this report we assume that the IMF is invariant, though this is a fascinating area for future study.

For our 72 H α emitting galaxies, we found a median SFR of $5.2 \pm 0.8 M_{\odot} \text{yr}^{-1}$, with a maximum of $29 \pm 8 M_{\odot} \text{yr}^{-1}$ and a minimum of $0.8 \pm 0.3 M_{\odot} \text{yr}^{-1}$. This appears to match previously derived values for galaxies at similar redshifts (Swinbank et al. 2012). We calculated the specific star formation rate (SSFR), the SFR per unit stellar mass, for each galaxy and compared them to the results published in Feulner et al. (2005), as shown in Fig. 9. We assumed that the error in the SFR only came from the error in the calculated H α flux, which were derived from the 1σ uncertainty in the velocity from the Gaussian fit to the H α emission line.

Observations have indicated that there are two main modes of star formation which dictate the growth of galaxies: one which is relatively steady, takes place in disk galaxies and is described by a surprisingly simple relation between the SFR and stellar mass of a galaxy, and a starburst mode which are outliers to such a sequence and is interpreted as being driven by merging. In the former case it appears that the larger a galaxy is, the faster star formation occurs. This relationship is known as the galaxy main sequence, and it implies that the growth of these galaxies is a smooth, continuous process fuelled by the accretion of gas through the dark matter halo, minor mergers and the cold streams from the IGM. In fact, studies have found that as little as 1-3% of galaxies at this redshift are involved in mergers (Darg et al. 2010). Galactic interactions, such as mergers, provide a fresh supply of gas that

boosts star formation without as comparatively dramatic an increase in the stellar mass. If mergers were the dominant process for the growth of galaxies, there would be significant scatter in the SSFR- M_* relationship. The tightness of the scatter indicates that starbursts contribute only $\sim 10\%$ of the star formation taking place at the epoch of peak star formation $z \sim 1 - 2$ (Darg et al. 2010). This indicates that the majority of star formation within the ISM of galaxies at this epoch is driven by internal dynamical processes (Swinbank et al. 2012; Kereš et al. 2005). The star forming galaxies in our sample appear to lie on this main sequence, matching very closely with results published by Feulner (2005) shown in Fig. 9. This suggests that our galaxies double their mass over a typical timescale of 300-500 Myr up to $z \sim 1$ and halt upon reaching the so-called Schechter mass of $M_* \sim 10^{10.8-11} M_{\odot}$. The older galaxies are the most massive, but also have lower SSFRs. The typical evolution of a galaxy on the main sequence is to start at the top left of Fig. 9 and move along a line of constant SFR the bottom right, which is exactly what our galaxies appear to be doing. Galaxies below doubling line have not had enough time to double their mass by the present day. This suggests that the galaxies in our sample are not starbursts, but due to the dusty nature of these galaxies we cannot conclusively rule out that starbursts have been missed by the surveys we make use of.

Feulner summarises that the most massive galaxies with redshifts $z < 2$ are in a quiescent state, but at redshifts $z > 2$ the SSFR for massive galaxies increases by a factor of ~ 10 , reaching the time of their peak formation at $z \sim 1 - 2$. This large increase in the SSFR of the most massive galaxies suggests that at least a fraction of this population was formed in a period of efficient star formation in massive halos.

The SSFR of our galaxies match those reported in Feulner (2005) at a similar red-

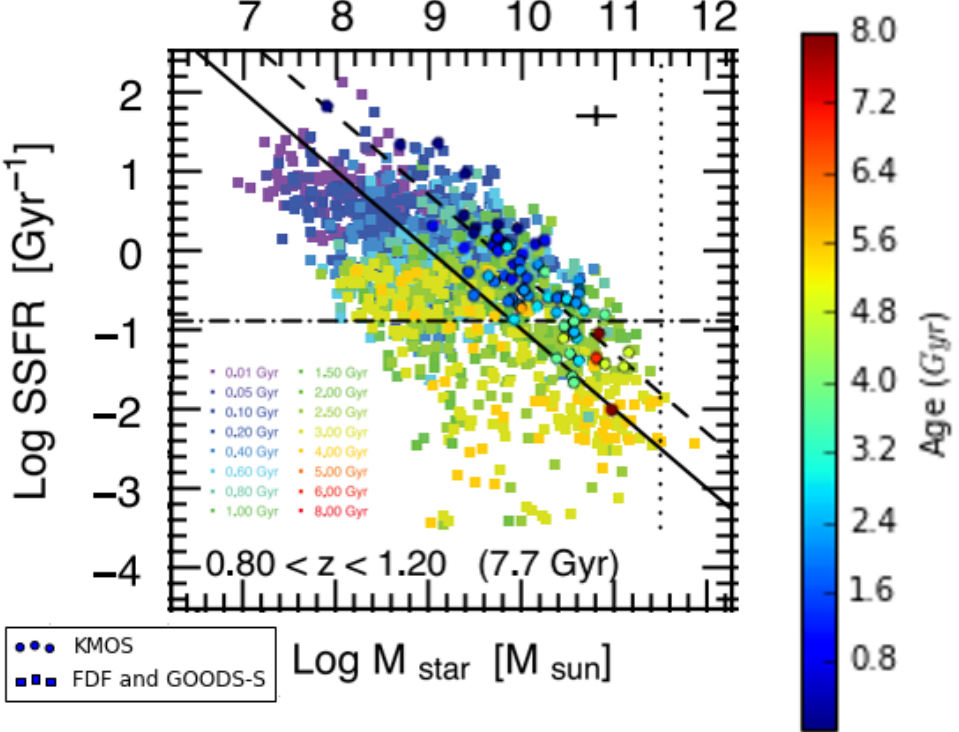


Figure 9: The SSFR as a function of stellar mass and redshift for galaxies taken from the FDF, GOODS-S, COMSOS and HiZELS surveys . Both the SFR and the mass are corrected for dust extinction. The circles in the foreground represent the SSFR of the galaxies analysed by KMOS and presented in this report, whereas the squares in the background represent the SSFR of galaxies presented in Feulner et al. (2005). Objects are coloured according to the age of the main component of the stellar population synthesis model fit to the photometry, ranging from 0.01 Gyr (purple) to 8 Gyr (red). The apparent large difference in age for our sample and those from Feulner are in fact purely aesthetic differences caused by differences in colour-schemes used in both cases. The colourbar should be applied to the KMOS data and the text-box guide for the FDF and GOODS-S data. The solid and dashed lines correspond to SFRs of $1 M_{\odot}$ and $5 M_{\odot}$ respectively. The dot-dashed line represents the SSFR needed to double a galaxy's mass between the redshift epoch and $z = 0$ (assuming constant SFR); the corresponding look-back time is displayed. The error bar in top right of the plot indicates the typical errors one might expect, while the dotted line roughly represents the high-mass cut-off of the local stellar mass function (Drory et al. 2004, 2005; Fontana et al. 2004). It should be noted that while the Feulner galaxies are sampled from $0.80 < z < 1.20$, the KMOS galaxies are sampled from $0.80 < z < 1.0$, which may cause systematic differences. This plot shows that the SSFR of galaxies analysed in this report agree with previous studies and therefore are indeed representative of typical star forming galaxies at $z \sim 1$ and further investigation into their physical properties may be take place.

shift, indicating that they are indeed representative of star forming galaxies at that redshift. Therefore studying them further in an attempt to place them in the wider context of galactic evolution is valid.

3.2.2 Metallicity

Stellar evolution and nucleosynthesis are the driving factors behind the creation of heavy elements. The first galaxies were formed from the condensation of the IGM and were composed primarily of H, D, ^3He , ^4He and ^7Li . Heavier elements than these

(up until ^{56}Fe) are produced via nucleosynthesis in stellar interiors. Interestingly, dwarf galaxies have such low metallicities that the analysis of their abundances can give indications into primordial conditions in the Universe. Heavy elements are released from stellar interiors in supernovae and other processes, such as accretion in binary pairs, while the rest is locked up in degenerate stellar remnants. The yield of elements released depends non-linearly on stellar mass; the larger the star, the hotter the interior and the heavier the produced

elements can be. As this created mass can be lost in the interactions between stars in binary systems, the yields for many elements can be very uncertain. This includes nitrogen (Prantzos 1998). The oxygen yield is fairly well determined, though the uncertainty is around a factor of 2. Due to the lifetimes involved, the majority of ISM enrichment comes from young, hot stars which produce and disperse heavy elements over the time scale of a few tens of millions of years. Cooler, long lived stars have ages similar to that of the galaxy and keep their nucleosynthesis products locked up inside them. Metal-rich areas are therefore indicators of vigorous star formation. Different elements are produced in varying quantities in different mass stars, so the ISM enrichment time will vary from element to element. Massive stars are the main producers of α -elements (elements produced via the triple alpha-process or the alpha process), so these elements will be ejected on shorter timescales. Before their dramatic deaths, massive stars ($M > 8M_{\odot}$) undergo mass-loss processes via stellar winds which reduces the yield of oxygen, but increases that of nitrogen, carbon and helium. In addition, supernovae and stellar winds may cause galaxy-wide mass loss, which will further influence ISM abundances.

As observations of H α emission indicate ongoing star formation, the metal content of galaxies can be viewed as an indicator of the sum of past star formation. The metal content of a galaxy has particularly important connotations when considered in tandem with stellar and gas masses, as relationships between these quantities constrain the nature of large-scale gas flows, in particular any deviations from closed box expectations (Swinbank et al. 2012).

As with the SFR in this report, most research into the metal content of high redshift galaxies focuses on the emission lines from HII regions, including the hydrogen recombination lines and collisionally excited forbidden lines from heavy elements,

including oxygen ([OIII], [OII]), nitrogen ([NII]) and neon([NeIII]) (Shapley 2011). These emission lines are commonly used to indicate the abundance of gaseous oxygen, expressed as $12 + \log(\text{O/H})$ (Asplund et al. 2004). In particular usage is the $N2$ index, defined as $\log([\text{NII}]\lambda6584/\text{H}\alpha)$. Pettini & Pagel (2004) find a linear relationship between $N2$ and the gas-phase abundance of oxygen, described by

$$12 + \log(\text{O/H}) = 8.9 + 0.5 \times N2, \quad (9)$$

which we shall use in this report. [NII] and H α are so close to each other in terms of wavelength that their ratio is not affected by reddening. A problem with using the $N2$ index is its saturation at $12 + \log(\text{O/H}) = 8.66$ (Asplund et al. 2004; Yoshikawa et al. 2010), which may affect some of our results with high integrated metallicity. Pettini & Pagel conclude that through use of the $N2$ calibrator, it is possible to estimate the abundance of oxygen to within a factor of ~ 2.5 at the 95 per cent confidence level.

[NII]/H α scales with O/H (Torres-Peimbert et al. 1989) due to their simultaneous creation during the CNO process within stars. One of the main advantages in using HII abundances to quantify metallicity is that they can be observed at large distances, giving us insights into the ISM in galaxies at their peak SFR. The drawback is that our view will be biased towards active star forming systems, systematically biasing our understanding of galaxy evolution (Kunth & Östlin 2000).

Metallicity and observations show that the SFRD was greatest between $z = 1-3$ (van de Voort et al. 2011), largely due to the most massive galaxies efficiently accreting gas from the halo which fuelled star formation. This gas can come from minor mergers or by cold streams from the IGM (Swinbank et al. 2012). A large proportion of the galaxy population at $z = 1-3$ have their ionised gas in large, rotating disks (Förster-Schreiber et al. 2009). The metal-

licity of the ISM can tell us a lot about the SFH at certain regions of the galaxies and also give an insight into their evolution. The metallicity of high redshift galaxies has been shown to decrease with galactic radius, indicating that they grow from the centre outwards (Swinbank et al. 2012). The mechanisms that control the metallicity in a galaxy involve many aspects of modern astrophysics, including the formation of massive stars, stellar winds, gas accretion and expulsion etc. (Kunth & Östlin 2000). Roughly speaking, metallicity scales with galactic mass, so the lowest metallicities are found in dwarf galaxies.

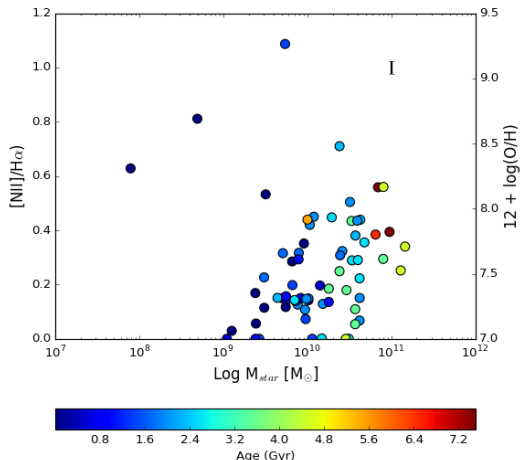


Figure 10: The integrated metallicities of the 72 galaxies H α emitting galaxies at $z \sim 1$, calculated as the ratio of the observed [NII] and H α line fluxes. **(Left)** The full sample and **(Right)** the galaxies with $NII/H\alpha < 1.2$. The data points are coloured according to the age of the main component of the stellar population synthesis model fit to the photometry, ranging from 0.0 Gyr (blue) to 7.2 Gyr (red). Galaxies with $NII/H\alpha = 0$ have no observed NII emission. The majority of the galaxies follow the trend of stellar mass and metallicity increasing with age, indicating that star forming galaxies undergo long periods of steady star formation. As the rate of gas accretion decreases and supernovae continue to occur, the integrated metallicities gradually increase.

We calculate an average galaxy-integrated $[NII]/H\alpha$ ratio to be 0.30 ± 0.05 and an average $12 + \log(O/H) = 8.52 \pm 0.03$. This value is in good agreement with the 8.58 ± 0.07 quoted in Swinbank et al. (2012) for star forming galaxies at a similar redshift, and fits

with the redshift-metallicity relationship in Yuan et al. (2013). This increase in metallicity shows that the pollution of the ISM by heavy materials formed in the heart of massive stars slowly overcomes the purification by the accretion of neutral gas from the IGM, as the efficiency and rate of accretion declines and more stars reach the end of their lives. We also see evidence for this in Fig. 10, which shows the relationship between metallicity, age and stellar mass. A graph relating $[NII]/H\alpha$ and $12 + \log(O/H)$ is shown in the appendix.

While the $[NII]/H\alpha$ ratio is not perfect, it is sensitive to shock excitation for instance (Kewley & Dopita 2002), our ratios are consistent with star formation throughout the rotation dominated galaxies we find an average $[NII]/H\alpha$ of 0.523. However this falls to 0.28 ± 0.08 once we discount HiZ_z1.301, which has a calculated $[NII]/H\alpha$ value of 3.26. The rotation dominated systems have an average $[NII]/H\alpha$ of 0.25 ± 0.03 . This suggests that on average there is not much difference between the metallicities of dispersion and rotation dominated galaxies at this redshift.

We shall discuss our findings for spatially resolved metallicity gradients in Section 4.1, once we have described how these observations were made in the following sections.

3.3 Internal Dynamical Observations

We measured the internal properties of the galaxies in much the same way as we measured the integrated properties as discussed in Section 3.1, but rather than analysing the emission spectrum for the integrated galaxy we did so on a pixel by pixel basis. The emission features in the spectrum of each pixel give us information about the physical conditions of each pixel, which when analysed together tell us about the galaxy-wide variation of these properties. We created two dimensional maps

of H α emission (and therefore star formation), [NII] emission, relative velocity and velocity dispersion. Maps were created in the calculation of the spin parameter and metallicity gradients, but are not presented in this report. We achieved this by initialising empty 14×14 arrays and populating each coordinate with information depending on whether or not H α emission had been observed, again employing Eq.3 and a 7σ catch. This allowed us to have a clearer idea of a star forming region's spatial extent and their internal properties. A comparison of a narrowband image and H α flux map is shown in Fig. 11.

We shall now use these flux maps to calculate metallicity gradients in our galaxies.

4 Results and Discussion

4.1 Spatially Resolved Metallicity Gradients

Spatially resolved [NII]/H α measurements have only been made for high redshift galaxies ($z \sim 1.5 - 2.5$) in the last few years. Observations have found that high-redshift galaxies have highly negative metallicity gradients, indicating strong SFR in the bulge and gas accretion on the outer parts of the disk (Yuan et al. 2011). If these galaxies are to evolve into the spirals we see in the local universe, their gradients must flatten by $\Delta \log(\text{O/H})/\Delta R = 0.05 \text{ dex kpc}^{-1}$ in the intervening time. We here use our spatially resolved observations of H α and [NII] lines to calculate the distribution of chemical abundances.

Of our 72 galaxies, we found that 55 emitted strongly enough in H α and [NII] $\lambda 6583$ to allow spatially resolved studies of the metallicity gradients. We first located the galaxy centre using a median smoothing of the H α narrowband image, then plotted a preliminary graph of radius against [NII]/H α . Due to the pixelated nature of our samples, we often obtained many ratio values for a given radius. For

each unique radius, we calculated the average ratio with the error being the standard error of these values. We then further constrained our plots to have a maximum radius of R_{max} , which corresponds to the maximum observed radius of each galaxy taken from the integrated one dimensional rotation curve described in Section 4.2.

In Fig. 12 we show a sample of the spatially resolved metallicity gradients analysed; the rest of the figures and the gradients of individual galaxies are given in the Appendix. Of the 55 galaxies analysed, 22 had negative gradients whilst 28 had positive. Setting a standard catch of 10kpc rather than a tailored R_{max} raises the number of negatives up to 37, suggesting that our measured R_{max} is regularly an underestimate. In our approach we did not take the inclination of each galaxy into account when calculating the metallicity for different radius bins, which is likely a large source of error. Studies which do take the inclination into account, such as Swinbank et al. (2012), fare considerably better in collecting results consistent with inside-out growth. The fact that the integrated metallicities reported here match the aforementioned paper but the spatially resolved gradients do not, suggests that inclination error is indeed the cause for this disparity.

The R_{max} clipping receives some vindication when we calculate the average $\Delta \log(\text{O/H})/\Delta R$ gradients. For the 10kpc clipping we find $\Delta \log(\text{O/H})/\Delta R = -0.26 \pm 0.05 \text{ dex kpc}^{-1}$, whereas for the R_{max} clipping we find $\Delta \log(\text{O/H})/\Delta R = -0.026 \pm 0.019 \text{ dex kpc}^{-1}$. This suggests that our choice of a R_{max} was the correct course as this result matches well with Swinbank et al. (2012), which finds a value of $-0.027 \pm 0.05 \text{ dex kpc}^{-1}$, and Queyrel et al. (2012) for starbursts at $z \sim 1$. Our theory is that the galaxy inclination error systematically affected the gradients of each galaxy, but as galaxy inclination is random the effect is almost nullified when considering a large galaxy population as a whole.

zcos_z1_172

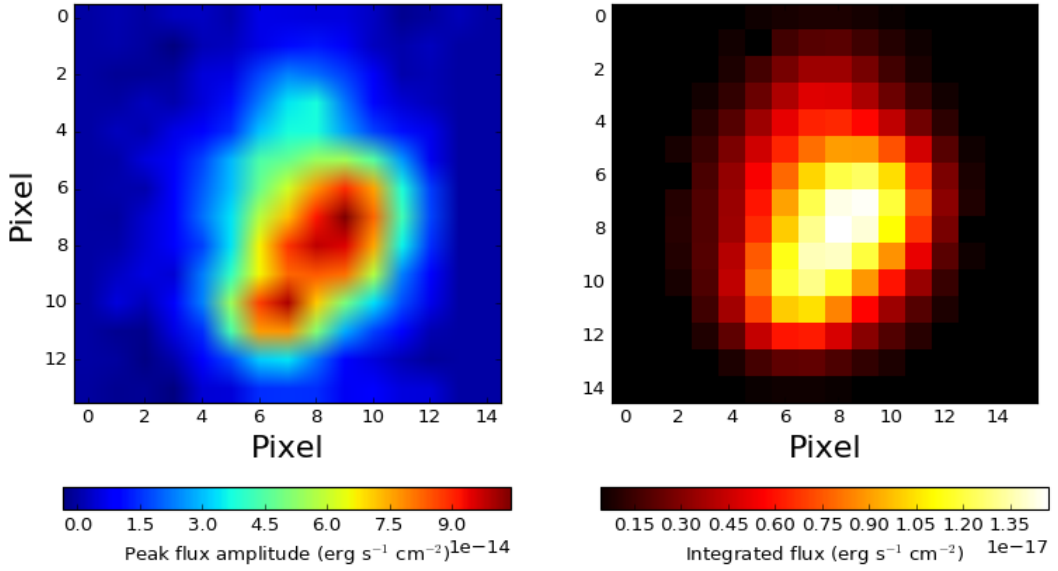


Figure 11: (Left) Smoothed raw image of the $\text{H}\alpha$ emission of zcos_z1_172 and (Right) the integrated $\text{H}\alpha$ flux per pixel according to the Gaussian fit of each pixel's emission spectrum. Pixels with a $\text{H}\alpha$ emission with $S/N < 7$ are set to black. As $\text{H}\alpha$ can be used as a proxy for ongoing star formation, we can see that the galaxy displays heavy star formation in a galactic central region and reduced star formation at higher radii. Calculating the flux per pixel makes it easier to discern the star forming regions from the background and begin to identify structure within the galaxy.

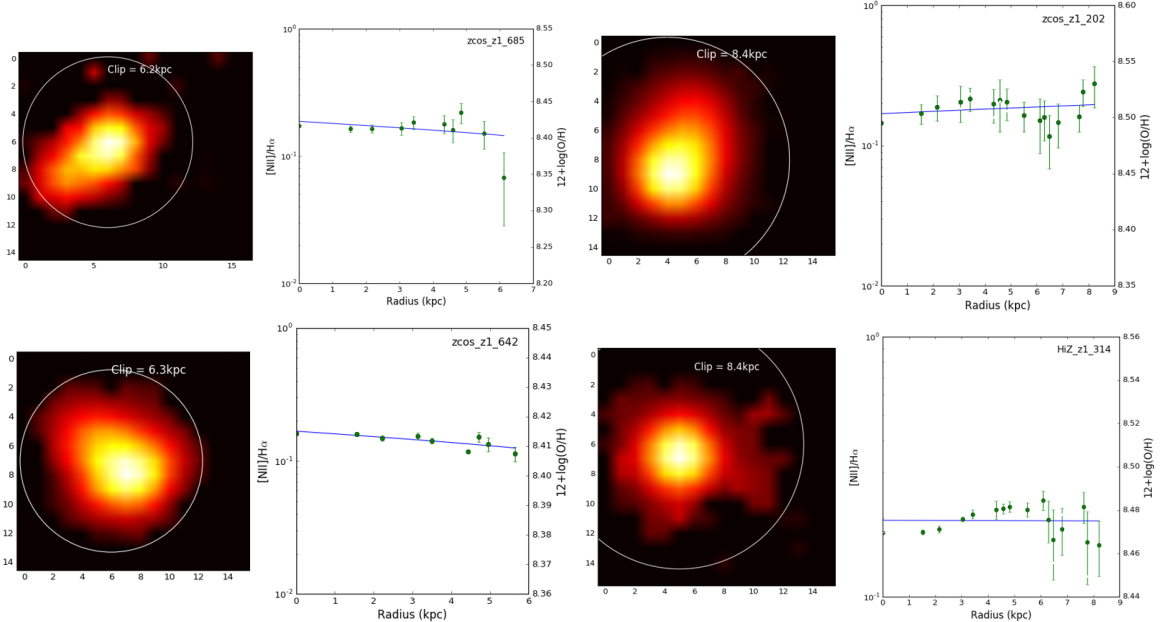


Figure 12: Metallicity gradients for four out of the 55 galaxies for which spatially resolved measurements could be made, the rest are displayed in the Appendix. (Left) Median smoothed $\text{H}\alpha$ flux maps. The solid white circle represents the area from which the $[\text{NII}]/\text{H}\alpha$ ratios were extracted, the radius being determined by the maximum observed radius during our measurement of a 1D integrated rotation curve in Section 4.2. (Right) the ratio $[\text{NII}]\lambda 6583/\text{H}\alpha$ plotted against the physical radius. The blue line represents an optimised linear fit. Only half of the gradients were negative, which is contrary to expectation of the majority being negative given our expectation of growth starting at the bulge and working outwards. Positive gradients could be accounted for by the effects of inclination.

The considerably large error can also explained by this.

Our result fits in well with the GIMIC simulation's predicted metallicity gradients, as a function of redshift (Crain et al. 2009; McCarthy et al. 2012), which finds that the steepness of gradient peaks at $z \sim 3$ where gas accretion from the IGM is at its most efficient, and then grows shallower by a factor of 2 by $z = 0$. According to the simulation, this takes place as the rates of gas accretion decline and the outer disk becomes more polluted with heavier elements.

In the next section we shall use the emission spectrum of each pixel to determine the internal dynamics of our star forming galaxies and see how they affect star formation and chemical abundances across the disl.

4.2 *Rotational Velocity and Velocity Dispersion*

To create a 2D velocity field for the 72 H α emitting galaxies in our sample, we made use of the equation describing the Doppler shift of spectral features due to motion:

$$v_{rel} = c \left(\frac{\lambda_0}{\lambda} - 1 \right) \quad (10)$$

with v_{rel} being the velocity of the pixel relative to the galactic centre, λ_0 the wavelength of the H α line at the centre of the galaxy and λ the wavelength of the H α line at each pixel. We used the median smoothing technique described in Section 4.1 and Fig. 4 to find the galaxy centre, created a 3×3 grid about the pixel and obtained the integrated emission spectrum for the region, setting λ_0 to be the wavelength of H α for this spectrum. This was done to minimise the effects of Doppler broadening on any one pixel's emission line and the uncertainty in the location of the galactic centre. Fig. 13 shows the velocity fields for a sample of our galaxies.

We obtained integrated one-dimensional rotation curves by taking our velocity fields and rotating about the apparent axis of rotation. We did this using the python

function `scipy.ndimage.interpolation.rotate`, with the order of spline interpolation set to 1. An example of the rotation technique employed can be seen in Fig. 14. The function had the additional benefit of removing some of the pixels in our maps not directly connected to the main body of the galaxy, which made obtaining clean rotation curves easier. Once the axis of rotation was aligned parallel to the x-axis, we obtained the average velocity of each pixel, ± 1 pixels in the y axis, along the axis of rotation. This was then plotted against each pixel's distance from the centre.

We computed the error in the velocity by creating a velocity error field, analogous to the velocity field. The errors come from the standard 1σ uncertainty arising from the Gaussian fit to the H α line. We then rotated this field by the same angle as each corresponding velocity field and combined the errors in quadrature. This was compared with the standard error associated with the averaging of the vertical pixels along the axis of rotation (see Fig. 14) with the larger error carried through. The errors we computed seemed far smaller than has been found in previous work using a similar method, in particular Swinbank et al. (2012) finds errors $> 10 \text{ km s}^{-1}$ for a standard velocity measurement whilst we often found errors an order of magnitude smaller for similar velocities. It is possible that the errors were corrupted during the interpolation. We therefore decided to implement a minimum error of 10 km s^{-1} , which we felt was a fair approximation, in the instances that our calculated error was less than this. We would like in the future to return to this problem as we recognise the lack of scientific rigour in this approach.

We fit the rotation curves with a simple arctan model, described in Courteau (1997) as

$$v(r) = v_0 + \frac{2}{\pi} \arctan(R), \quad (11)$$

where $R = (r - r_0)/r_t$, v_0 is the velocity

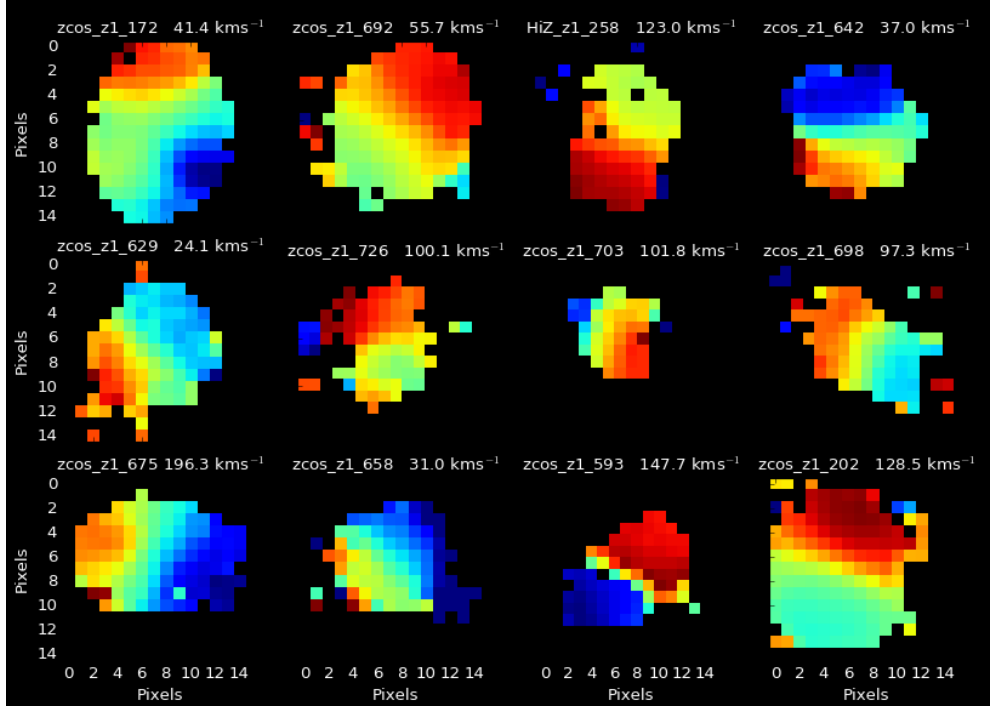


Figure 13: Spatially resolved 2D velocity fields of a 12 galaxy sample from our 72 H α emitters. The maximum observed velocity for each galaxy, indicated at the top of each plot, was obtained by creating a one-dimensional rotation curve based on the dynamical centre and extremities. They have not been inclination corrected. For the full selection of velocity fields see the Appendix. These velocity maps are consistent with being large, rotating disks.

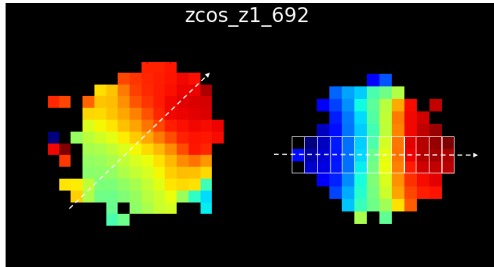


Figure 14: An example rotated velocity field using a spline interpolation technique. The white dashed arrow in both cases represents the axis of rotation. Left is the original field, right is rotated field with the axis of rotation parallel to the x-axis. Each vertical grid represents the area over which the average velocity value was computed.

at the centre of rotation, r_0 is the spatial centre of the galaxy, v_c is the asymptotic velocity, and r_t is the transition radius between the rising and flat parts of the curve. We used the same optimisation function as is used in Section 3. We compared $v(R_{max})$ (where R_{max} is the maximum observed spatial distance from the galactic centre) with v_c to determine whether we had detected a turnover in the rotation curve (as is ex-

pected due to the existence of the dark matter halo), setting $v(R_{max}) > 0.7v_c$ to be the required criteria. We found that 60 of our galaxies have smooth velocity gradients and one-dimensional rotation curves, dynamics consistent with their ionised gas being in large rotating disks. A sample of these rotation curves are displayed in Fig. 15. This agrees with previous studies of star forming galaxies at $z \sim 1 - 2$, which suggest that the majority of these galaxies are indeed rotating disks (e.g. Förster-Schreiber et al. 2009; Swinbank et al. 2012). We found that half of these galaxies have $v(R_{max}) < 0.7v_c$, indicating that their extremities are not visible in H α because star formation is predominantly taking place close to the bulge.

We corrected for galaxy inclination, $v_{cor} = v_{obs}/\sin(i)$, using the formula for an oblate spheroid given in Holmberg (1946):

$$i = \cos^{-1} \sqrt{\frac{(b/a)^2 - q_0^2}{1 - q_0^2}}, \quad (12)$$

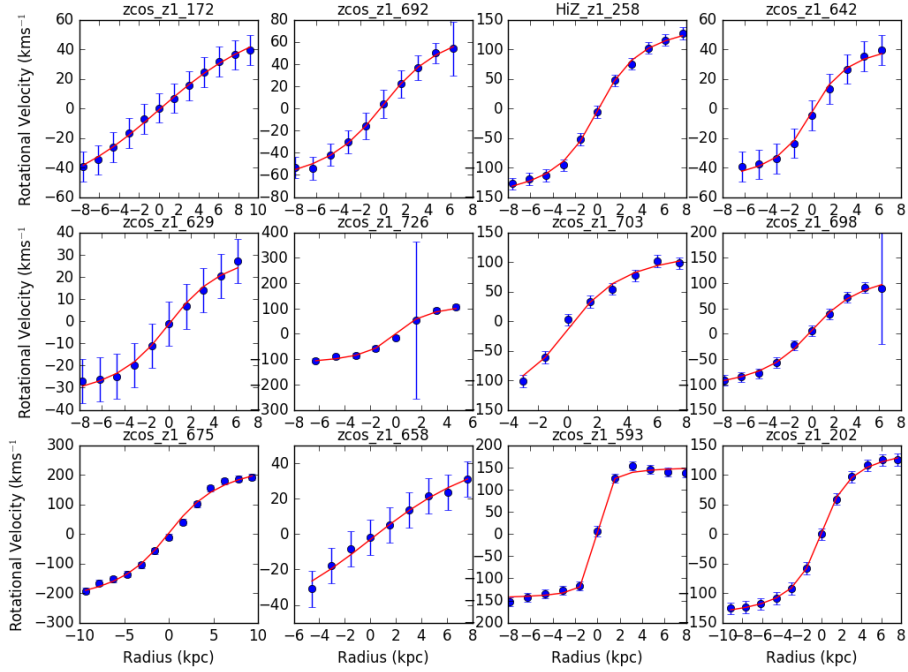


Figure 15: The integrated one-dimensional rotation curves for a sample of 12 galaxies, which all show strong velocity gradients in their H α dynamics. Overlaid is the best-fitting arctan model from Courteau (1997). The rotation curves were extracted from the 2D velocity maps shown in Fig. 13 from a ~ 1.5 kpc slit across their axes of rotation. These galaxies show strong velocity gradients, indicative of rotating disks.

where the semi-major (a) and the semi-minor (b) axes are determined from an isophotal fitting of the galaxy image and q_0 is the axial ratio of a galaxy viewed edge on. As discussed in Hall (2012), the value for q_0 for late-type spiral galaxies usually ranges from 0.13 to 0.2, though S0 galaxies can be as high as 0.8. We will adopt $q_0 = 0.13$; using $q_0 = 0.2$ instead makes very little difference to our results.

We adopted an error of 30% in the inclination angle and discounted the four galaxies with $i < 25^\circ$ from consideration due to the large uncertainties involved.

We also made our rotation curves symmetric about the x and y axes to ensure that we were obtaining the correct value for $v(R_{max})$.

We calculated the velocity dispersion of a star forming region using the equation

$$v(\sigma) = c \left(\frac{\Delta\lambda(\sigma)}{\lambda} \right), \quad (13)$$

where $\Delta\lambda(\sigma)$ is the Gaussian RMS of the H α emission line and λ is the wavelength of the line. We display a sample of the dispersion maps in Fig. 16. For the rotating galaxies we found $\sigma = 46 - 146$ km s $^{-1}$ with a median of 70 ± 4 km s $^{-1}$ and for the non-rotating galaxies we found $\sigma = 43 - 322$ km s $^{-1}$ with a median of 70 ± 30 km s $^{-1}$.

For the galaxies found to be rotating disks, only 23 had $v(R_{max}) > v_c$. For these, we calculated the ratio between rotational support and thermal pressure, v/σ . A value less than 1 is typically taken to indicate that a galaxy's dynamics is dominated by thermal motions. For our sub-sample of galaxies with $v(R_{max}) > 0.7v_c$, we find $v_{max} = 30 - 390$ km s $^{-1}$ with a median of 150 ± 20 km s $^{-1}$ and $v/\sigma_0 = 0.47 - 3.21$ with a median of 2.0 ± 0.2 . Three quarters of our rotating galaxies have $v/\sigma > 1$, while the other quarter have $v/\sigma < 1$.

The galaxies which have $v(R_{max}) < 0.7v_c$, we found $\sigma = 46 - 146$ km s $^{-1}$ with

a median of $67 \pm 5 \text{km s}^{-1}$. This is in agreement with the other rotating galaxies with a more clearly defined $v(R_{max})$. Due to the poor turnover in these galaxies' rotation curves, $v(R_{max})$ and v/σ can only be considered lower limits of the true values. We found $v = 15 - 349 \text{km s}^{-1}$ with a median of $80 \pm 20 \text{km s}^{-1}$ and $v/\sigma = 0.22 - 4.5$ with a median of 0.2 ± 0.2 .

Combining the dynamical information gathered in this section together, we find that roughly four out of five of our H α emitting galaxies show clear velocity gradients and have clear central maxima in corresponding dispersion maps, and can be classified as 'rotation dominated'. For the galaxies which have well-defined $v(R_{max})$, we find the v/σ to be 2 ± 0.2 , adding further credence to our theory that these are rotation dominated. The remaining one-fifth of our galaxies have no evidence for rotation and instead seemed to be characterised by large, ubiquitous velocity dispersion and are thus classified as 'dispersion dominated'. We found that the dispersion dominated systems had a noticeably lower median stellar mass ($8.5 \times 10^9 M_\odot$) than the rotation dominated systems ($1.2 \times 10^{10} M_\odot$), in line with studies (Förster-Schreiber et al. 2009; Law et al. 2009) which suggest that lower stellar mass systems have higher gas fractions and tend to have negligible rotation. Our dispersion dominated objects have a range of ages (0.0062-7.5 Gyr) and include a few young, likely gas rich, star forming systems in the early stages of formation. HiZ_z1_290 is the youngest at 6.3 Myr, with a stellar mass of $4.9 \times 10^8 M_\odot$ (significantly lower than the median) and a calculated dynamical mass of $1.04 \times 10^{12} M_\odot$, suggesting a large reservoir of molecular gas. Older dispersion dominated systems could be late stage galaxy mergers.

The median value of v/σ , 2 ± 0.2 , is significantly lower than the values of $\sim 10\text{-}20$ observed in local spiral galaxies (Förster-Schreiber et al. 2009). This agrees with

previous results which indicate that in general the ISM of high-redshift galaxy is much more turbulent than the thin disk of a local galaxy and may be assumed to have a higher gas fraction ($f_{gas} = 20 - 80\%$) (Daddi et al. 2010; Tacconi et al. 2010; Geach et al. 2011; Swinbank 2011). We shall explore gas fractions in the following section. This higher gas fraction may be postulated to be the reason that high-redshift galaxies have significantly higher star formation rates. The evidence here agrees with the broad-stroke evolutionary path between high-redshift and local spiral galaxies (Förster-Schreiber et al. 2009): large scale structure in the universe formed from the gravitational instability of the initial fluctuations in the density of the early universe, which led to the formation of galaxies at the centre of dark matter halos. These galaxies grew, with star formation fuelled by the accretion of gas through the halo and cold streams from the IGM and peaking at $z = 1 - 3$, (Bournaud & Elmegreen 2009; Swinbank 2012; van de Voort 2012). This gas causes the large velocity dispersions observed in our results. By $z \sim 1 > 90\%$ of the stellar mass seen today in the most massive galaxies ($10^{11} M_\odot$) had been assembled (e.g., Dickinson et al. 2003; Fontana et al. 2003). From this epoch of peak formation, we observe a dramatic reduction in the SFR- ρ of the universe. The low velocity dispersion and SFR in local spirals suggests a lower gas fraction, which indicates that the accretion of gas through the dark matter halo and cold streams from the IGM has slowed. Possible mechanisms for this reduction in gas accretion include preventative and ejective feedback, where gas is stopped from either entering the galaxy or initiating star formation and where gas is ejected from the galaxy respectively (Kereš et al. 2009). Ejective processes may explain how the SFR in massive galaxies, such as those in our sample, are quenched. An example of a possible ejection pathway is via the high-

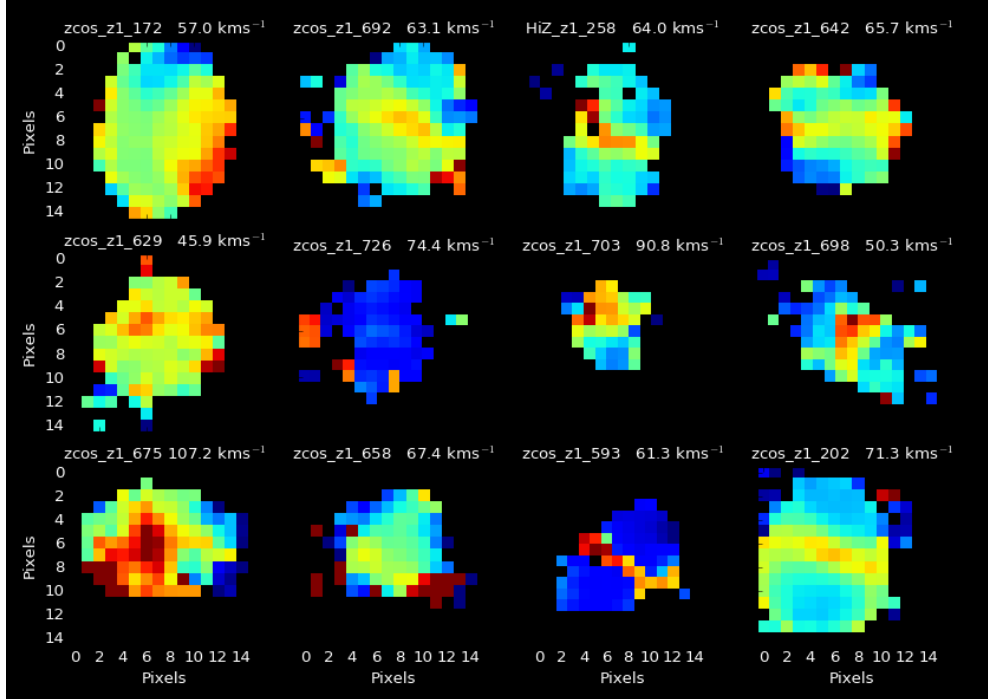


Figure 16: The velocity dispersion fields of a sample of the galaxies observed in this report. The median dispersions are displayed above each plot. Most of these galaxies appear to have the dispersion peaking in the dynamical centre and have symmetrical, smooth rotation curves (see Fig. 13) indicating that they are indeed rotating. These galaxies have high dispersions relative to their rotational velocities, indicative of large gas fractions in the galaxies.

energy jets emitted by supermassive black holes following gas accretion (Di Matteo et al. 2005). An example of a preventative mechanism for galaxies with large dark matter halos is ‘virial shock heating’, which may prevent gas from cooling sufficiently to form stars (Gabor et al. 2010).

Previous studies of star forming, rotating galaxies at $z \sim 1 - 2$ generally find $v/\sigma \sim 0.2 - 1$ (Daddi et al. 2010; Tacconi et al. 2010). Our sample at $z \sim 0.8 - 1$ with $v/\sigma \sim 0.47 - 3.2$ could be seen as the evolutionary ‘missing link’ between the high dispersion galaxies at $z \sim 1 - 2$ and the low dispersion local spiral galaxies. Shapley (2011) reports that high velocity dispersions appear to be commonplace for star forming galaxies at high-redshift. The causes of this is still a matter of debate. Genzel et al. (2011) reviews possibilities, which include the conversion of potential energy to kinetic as accreted matter falls inwards and collisions between clumps. Alternatively, Lenhart et al. (2009) suggests

that turbulence is strongly influenced by stellar winds and supernovae feedback.

Our spatially resolved H α maps (Figs. 13, 15 & 16) appear to indicate clumpy morphologies, which are commonly observed in similar galaxies (Förster Schreiber 2009; Genzel 2008). Clumps are found in both rotation and dispersion dominated systems and appear to generally follow the velocity fields of rotating galaxies, indicating that these clumps are not distinct systems that have been accreted into a larger body. The realness of our observed ‘clumps’ which are disconnected from the main star forming body need to be further investigated. As H α regions indicate star formation, it is possible that a H α derived field does not show the entire baryonic component of a galaxy. High dispersion regions disconnected from the main star forming body could indeed be the highly turbulent infalling clumps discussed by Genzel et al. (2011), surrounded by a star forming ‘bald patch’ in

the galaxy. Alternatively as the majority of these objects are close to the edge of the field of view, it could be that these regions are in fact optical aberrations caused by dithering or other smearing effects. Indeed these regions seem to have dramatically different velocities to the rotation of the main galaxy body, indicating that if they are real, they are potentially distinct star forming bodies that have been gravitationally captured by the larger galaxy. One way of checking whether the clumps are real would be to compare our $H\alpha$ images with optical images taken by the Hubble Space Telescope (see Fig. 23 in the Appendix), as the clumpy regions should be visible in the optical light. Ultimately we had to prioritise other aspects of this report, so we shall assume the clumps here are real and discuss them further whilst admitting that validation of the realness of 'disconnected' clumps is required before any definitive statements about their role in the evolution of star forming galaxies can be made.

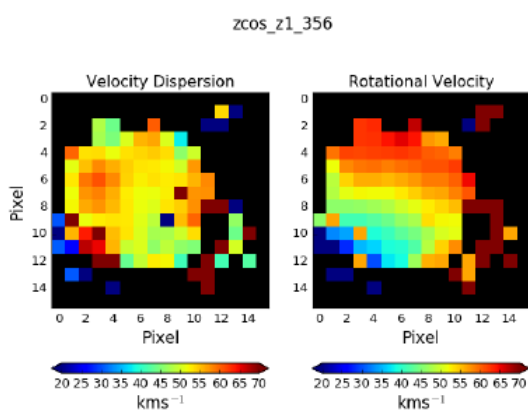


Figure 17: (Left) Dispersion and (Right) velocity field for the star forming galaxy zcos_z1_356 derived from $H\alpha$ observation. The colorbars indicate that the colours are saturated beyond the upper and lower bounds. The dispersion map shows areas of high turbulence in the galaxy interior, which appear to have similar rotational velocities to the surrounding galaxy, indicating that these are distinct star forming regions that have not been accreted, but instead are clumps which form from the collapse of gas clouds. Outside the main body of the galaxy we find other high turbulence regions, the realness of which is debatable as they could be optical aberrations associated with dithering.

The clumps we observe (an example of which is shown in Fig. 17), external and internal, appear to be on the scale of a few kpc which matches the predicted Jeans length for fragmentation of highly turbulent gas (Genzel et al. 2008). The exact role of clumpy structures in the growth and evolution of star forming galaxies is an area of ongoing research. Numerical simulations suggest that clumps start life at the edges of galaxies and travel inwards to participate in the coalescence and growth of the bulge over a timescale of $\sim 0.5\text{--}1\text{Gyr}$ (Dekel, Sari & Ceverino 2009). Alternatively the feedback associated with star formation (e.g. supernovae, stellar winds) may break apart these clumps as they migrate inwards and instead cause them to participate in the build-up of mass in the disk (Shapley 2011).

The distribution of mass in the disk combines with the rotational velocities to create a galaxy's angular momentum, which can be a key piece of data when constraining evolutionary models. We shall explore this in the next section.

4.2.1 Angular Momentum

The morphologies of galaxies appear to be inherently linked to the evolution of their angular momenta. Late type galaxies are very efficient at retaining specific angular momentum (j), and early types proficient at losing it. The $j - M_\star$ plot is therefore a key tool for assessing and interpreting any model of galaxy formation.

We calculated the stellar contribution angular momentum of our rotating, star forming galaxies as $J_\star = M_\star R_{max} v(R_{max})$, where M_\star is the stellar mass. The specific angular momentum is the product of the size of the disk and its rotational velocity, and for a fixed circular velocity with redshift it supplies information into the relationship between star formation in the disk and the spin of the halo (e.g. Tonini, Lapi & Salucci 2006). Research has suggested that the specific angular momentum of disks is higher by a factor of 1.4 ± 0.3

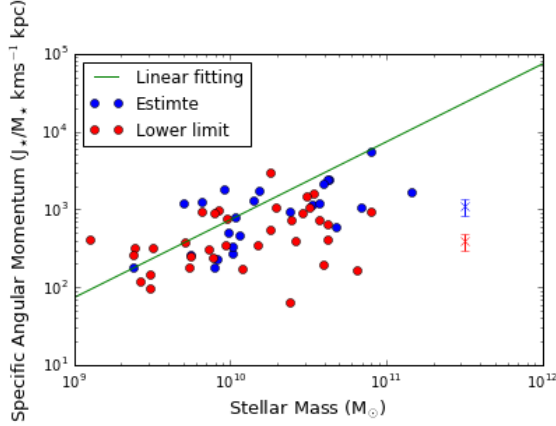


Figure 18: The specific stellar angular momentum of star forming galaxies and their relationship with redshift. Blue datapoints represent estimates as they are calculated from well-defined rotation curves, whereas red datapoints represent lower limits as they were derived from incomplete rotation curves. The blue and red error bars represent the median values and median errors for estimates and lower limits respectively. There appears to be a strong correlation between J_*/M_* and M_* , as shown by a linear fitting of the ‘estimate’ data points. For the estimates we find an average j of $(3.8 \pm 0.7) \times 10^{25} \text{ km s}^{-1} \text{ kpc}$ and for the lower limits an average of $(1.9 \pm 0.3) \times 10^{25} \text{ km s}^{-1} \text{ kpc}$.

at $z = 0$ than $z = 2$ (Navarro & Steinmetz 2000). For these disks to be connected evolutionarily, there must take place a gain in angular momentum. Scenarios for this include the loss of material with low angular momentum through outflows, or the decoupling of the galaxy disk from the halo, which acquires angular momentum via gas accretion (Swinbank et al. 2010).

For the our well-defined rotation curves we find an average j of $(3.8 \pm 0.7) \times 10^{25} \text{ km s}^{-1} \text{ kpc}$ and for the poorly defined rotation curves an average of $(1.9 \pm 0.3) \times 10^{25} \text{ km s}^{-1} \text{ kpc}$. We find evidence for a gain in specific angular momentum over the evolution of a star forming galaxy in Fig. 18, where we see that stellar mass increases with specific angular momentum. Assuming that these galaxies are on the same evolutionary pathway, this suggests that as a galaxy accretes gas from the IGM and through the dark matter halo to fuel star formation, there is a build-up of stellar mass in the outskirts of the disk and a gain

in angular momentum.

The $j - M_*$ plot is a physics-based alternative to the traditional Hubble tuning fork diagram, as galaxies of intermediate types have intermediate j at each M_* . It is found that $j \propto M_*^\alpha$, with $\alpha \sim 6$, and that spirals and ellipticals are offset by a factor of ~ 5 (see Fig. 19) (Fall & Romanowsky (2013), hereafter F&R).

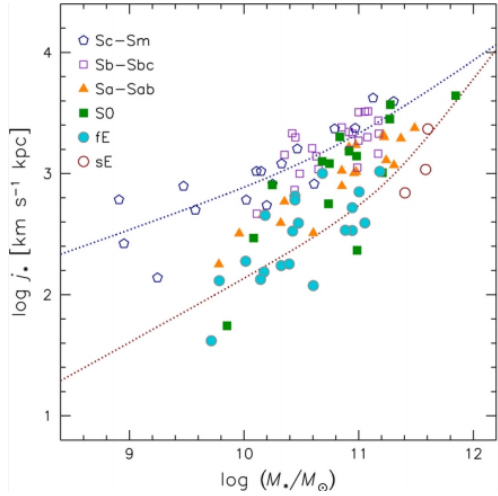


Figure 19: (From Fall & Romanowsky 2013) Specific angular momentum plotted against mass for entire galaxies (disk plus bulge) of different morphological types. The dotted curves represent our simple model of variable retention of specific angular momentum in a Λ CDM cosmogony with fractional net angular momentum factor $f_j = 0.8$ (upper curve) and $f_j = 0.1$ (lower curve).

We find by overlaying Figs. 18 and 19 that the majority of our rotation dominated galaxies lie in the same $j_* - M_*$ parameter space as the late type spirals in F&R. This confirms our suspicion that the majority of our H α selected, star forming galaxies are indeed spirals and that these galaxies dominate star formation at high redshift. As the errors involved in the calculation of the stellar mass are large it would be unreasonable to try to assess each galaxy’s exact type individually, but it is statistically valid for us to comment on the general nature of the population at large.

F&R concludes that many of the processes affecting galaxies will change j and M simultaneously. For example in mergers there is generally a decrease in j (by the

vector cancellation of spins) while M increases. If elliptical galaxies formed mainly by mergers, this could account for much of their offset from disk-dominated galaxies in the j - M diagram. Outflows, which decrease M , can increase or decrease j , depending on whether they remove material predominantly from the inner or outer parts of galaxies. As the majority of our ‘estimate’ class galaxies lie close to the line as best fit, we conclude that few, if any, of the galaxies in our sample are mergers.

In the next section we shall investigate the dynamical parameter λ_R , which provides another route into the investigation of rotational and thermal support, and its relationship with stellar content of galaxies.

4.2.2 Spin

With the advent of integral field spectroscopy, the ATLAS^{3D} team (Emsellem et al. 2011) developed a new parameter λ_R to act as a proxy for specific angular momentum. We shall here describe some of its uses and present our results into its relationship with M_\star . It is defined as

$$\lambda_R = \frac{\sum_{i=1}^N F_i R_i |V_i|}{\sum_{i=1}^N F_i R_i \sqrt{V_i^2 + \sigma_i^2}}, \quad (14)$$

where F_i is the flux, V_i is the velocity, σ_i is the velocity dispersion and R_i is the radius of the i th pixel. This parameter was originally used to classify early-type galaxies as either fast or slow rotators (Cappellari et al. 2011). It was discovered that spiral and lenticular galaxies tended to be fast rotators, whereas ellipticals could belong to either. Similar to the $j - M_\star$ plane in the previous section, it has been found that different morphologies of galaxy occupy different parameter spaces for $\lambda_R - c$ where $c = R_{90}/R_{50}$ - the ratio of the radii enclosing 90% and 50% of the light. This gives us an indication of rotational support and the concentration of the stellar population. Analysis of this parameter space provides constraints for evolutionary models of

spiral galaxies. An example of this is the evolution of late-type spirals into S0s. For this to take place, $\lambda_R - c$ tells us that spirals must undergo processes that heat the disks, reduce rotational support and also inflate the bulge, increasing the concentration (Querejeta et al. 2015). A possible pathway for this is for the galaxy to interact with neighbouring bodies through minor mergers and tidal interactions. This dynamically heats the disk and channels gas to the bulge, fuelling centralised star formation (Fogarty et al. 2015).

We find a median value of 0.55 ± 0.04 and that λ_R does not strongly correlate with stellar mass, which is in agreement with Burkett et al. (2015). This indicates that a galaxy’s spin receives contributions from a wider array of sources, such as the dark matter halo. There is significantly more scatter in Fig. 20 than Fig. 18, indicating that in this case the suggested usage of λ_R as a proxy j is limited. In addition, λ_R does not appear to correlate with SFR nor SSFR.

In the following section we shall calculate the dynamical masses of our KMOS observed galaxies using the dynamical information we have gathered in this section.

4.2.3 Dynamical Mass

Following the virial theorem we calculate a galaxy’s dynamical mass as

$$M_{dyn} = \frac{Rv_{obs}^2}{G \sin^2 i} + \frac{c\sigma^2 R}{G}, \quad (15)$$

where R is the maximum observed radius, v is the velocity at this radius, $\sin(i)$ is the inclination correction, σ is median velocity dispersion of the spatially resolved velocity dispersion map and c is constant. For rotation dominated systems we shall take $c = 5$, which comes from assuming isotropic velocity dispersion, and for the rotationless dispersion dominated systems we take $c = 10$. A source of error in this is that the velocity dispersions aren’t necessarily isotropic, which leads to significant

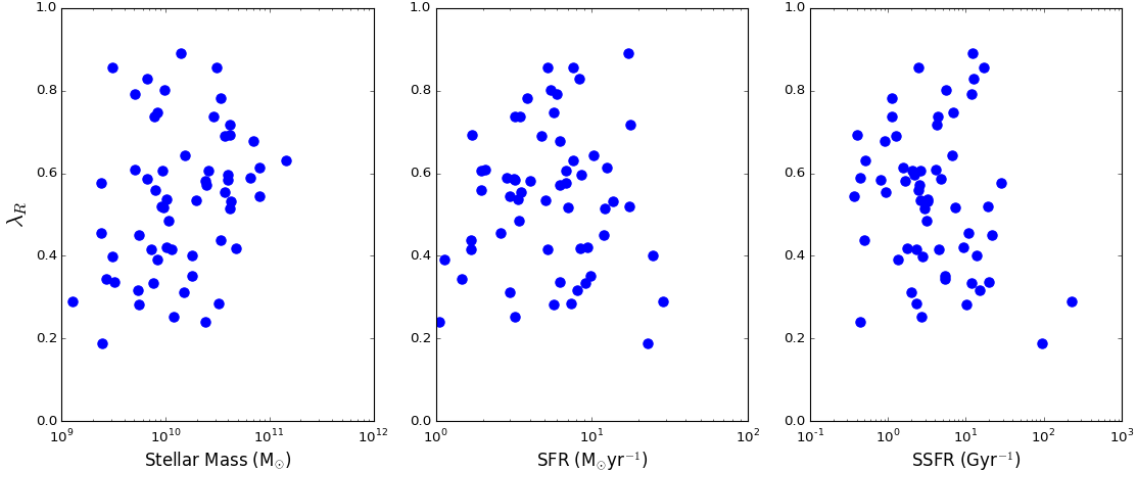


Figure 20: An investigation of the relationship between spin parameter λ_R and stellar mass, SFR and SSFR. We observe large scatter in all plots, indicating the lack of strong relationship between λ_R and the stellar content of star forming galaxies.

uncertainty. R comes from the small angle approximation, where the angle is the spatial resolution ($0.2''$) multiplied by the pixel separation of the galaxy centre and the edge and the arc length is the angular distance, D_A , which is related to D_L (Section 3.2.1) as $D_A = D_L/(z+1)^2$. Fig. 21 displays our plot relating the stellar and dynamical masses of star forming galaxies systems.

We find the median dynamical mass to be $(7.9 \pm 4.5) \times 10^{10} M_\odot$ for the well-defined rotation curves, $(3.5 \pm 1.5) \times 10^{10} M_\odot$ for the poorly defined rotation curves and $(5 \pm 11) \times 10^{10} M_\odot$ for the dispersion dominated objects. The large errors in these calculations indicate significant scatter. These masses are on average four times larger than their corresponding stellar masses indicating that a large fraction of a galaxy's mass is tied up in non-observable matter, be it dark matter or dust. The lower limits are considered such as their rotation curve have a limited turnover. As these curves cannot be completely traced with H α observations, this indicates that the farthest extents of baryonic regions in the galaxies have no ongoing star formation. As such, the matter we can observe only constitutes part of the complete disk, which may be observable in different wavelengths. Hence our calculation of the mass is only a lower

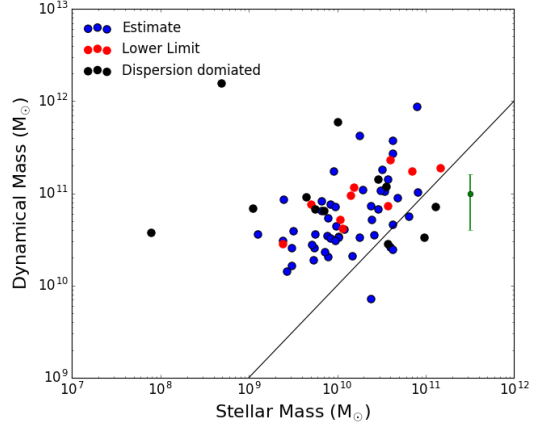


Figure 21: The relationship between the stellar and dynamical mass of our rotation dominated galaxies and 12 dispersion dominated galaxies. Blue dots represent estimates of dynamical mass using Eq. 15, where using an arctan fitting for rotation curves we find $v(R_{max}) > 0.7v_c$, red dots represent lower limits on dynamical mass, specifically when $v(R_{max}) < 0.7v_c$ and the black dots represent the dynamical mass of the dispersion dominated systems. The black line represents $M_{dyn} = M_\star$ and the green bar represents the median error of our dynamical masses, $6 * 10^{10} M_\odot$. We often find an order of magnitude difference between the stellar and dynamical mass, indicating that that stellar population contains only a small fraction of mass in high redshift galaxies. We find the median dynamical mass to be $(7.9 \pm 4.5) \times 10^{10} M_\odot$ for the well-defined rotation curves, $(3.5 \pm 1.5) \times 10^{10} M_\odot$ for the poorly defined rotation curves and $(5 \pm 11) \times 10^{10} M_\odot$ for the dispersion dominated objects. The large errors in these calculations indicate significant scatter.

limit. We find significant scatter in the relationship between dynamical and stellar

mass, though this may be due to the uncertainties in the measurement of the stellar mass.

We calculated the baryonic gas fraction as $f_{gas} = M_{gas}/(M_{gas} + M_\star)$ assuming that $M_{dyn} = M_{DM} + M_\star + M_{gas}$ and that dark matter constitutes 70% of the dynamical mass. We take this value from Schaller et al. (2015), which predicts through the hydrodynamical simulations of EAGLE a $73 \pm 6\%$ dark matter fraction within the central 9kpc of galaxies. This is an applicable value as the average radius at which we calculate the dynamical mass is 5.9 ± 0.2 kpc. These assumptions led to $f_{gas} = 1 - M_\star/(0.3M_{dyn})$.

Restricting our sample to our rotation dominated systems, we find an average $f_{gas} = 0.2 \pm 0.1$, However when we restrict our sample further to those with a positive f_{gas} , possibly indicating a general underestimation of the dynamical mass, we find an average $f_{gas} = 0.51 \pm 0.06$. Both of these values are in agreement with previous results that find $f_{gas} = 0.2 - 0.8$ for star forming galaxies at high redshift (Daddi et al. 2010; Tacconi et al. 2010). While the errors in each individual stellar mass is such that commenting on f_{gas} for each individual galaxy would be overly ambitious, we can say that the population on the whole appears to have a significant amount of gas with which to form stars. Similarly for the dispersion dominated galaxies with positive f_{gas} , we find the average to 0.8 ± 0.3 which leads us to the same conclusions as in the previous case. In the local universe the SFR per unit area is directly related to the Schmidt Law, $\Sigma_{SFR} \propto \Sigma_{gas}^N$ with N ranging from 0.9-1.7 (Kennicutt 1998). Tracing this relationship leads to a greater understanding of the conversion and efficiency of molecular gas to stars, with analysis at high redshift constraining this process at the epoch of peak formation. As the timescale of gas depletion is relatively short (compared with the Hubble time) ongoing star formation indicates a continuous

stream of gas being accreted onto the disk. Investigation of the Schmidt law requires knowledge of the spatial variation of stellar and gas mass across a galaxy, which is beyond the scope of this report. However this is a potential area for future study, as the spatial variation in the relationships between SFR and f_{gas} provide vital constraints into models of galaxy formation.

In future studies we would like to use less assumptions in the calculation of f_{gas} , perhaps by calculating M_{gas} separately through observations of the CO J($1 \rightarrow 0$) transition which serves as a tracer to molecular hydrogen gas (Young & Scoville 1996).

5 Conclusion

We have presented AO-assisted, spatially resolved spectroscopy of 102 galaxies at $z = 0.78 - 1.04$, selected from the HiZELS (Sobral et al. 2012) and COSMOS surveys and observed with the KMOS instrument at the VLT. Of these, 72 were found to be actively star forming. Our main results are summarised as follows:

- 1) Using integrated measurements of H α flux, we find a median SFR of $5.2 \pm 0.8 M_\odot \text{yr}^{-1}$, with a maximum of $29 \pm 8 M_\odot \text{yr}^{-1}$ and a minimum of $0.8 \pm 0.3 M_\odot \text{yr}^{-1}$. This appears to match previously derived values for galaxies at similar redshifts (Swinbank et al. 2012). We then calculated the SSFR of these galaxies and found that they lie on the galaxy main sequence by comparing them with results published in Feulner et al. (2005). This indicates that our galaxies are not starbursts, but are being continuously fuelled by gas accretion from the halo and cold streams from the IGM. This suggests that star formation within the ISM of these galaxies are driven by internal dynamical processes and not by extra-galactic interactions.
- 2) Using integrated measurement of the ratio [NII] $\lambda 6584/\text{H}\alpha$ and the N2 index proposed by Pettini & Pagel (2004) we find an average $12 + \log(\text{O/H}) = 8.52 \pm 0.03$.

This fits well with previous measurements for galaxies at similar redshift (Swinbank et al. 2012) and with the metallicity-redshift relationship described in Yuan et al. (2013), which finds a strong increase in galaxy metallicity after the time of peak formation, indicating that gas accretion has reduced or grown less efficient. We also find evidence for a linear fitting between stellar mass and metallicity, indicating that as star formation continues the short lived, massive stars of the population are continuously produced and continuously pollute the ISM with heavy elements during their supernova phase. Using the spatially resolved variations of $[NII]\lambda 6584/H\alpha$, we calculate an average metallicity gradient of $\Delta \log(O/H)/\Delta R = -0.026 \pm 0.019$ dex kpc $^{-1}$. The large error is likely due to the lack of inclination correction in our approach, though we have confidence in the value itself due to agreement with previous results (Swinbank et al. 2012). Our result fits well with the GIMIC simulation which measures $\Delta \log(O/H)/\Delta R$ as a function of redshift. GIMIC finds that metallicity gradient peaks at $z \sim 3$, where gas accretion from the IGM is at its most efficient, and then grows shallower by a factor of 2 by $z = 0$. This takes place as gas accretion becomes less efficient and the outer disk becomes polluted with heavier elements.

3) Using $H\alpha$ emission line dynamics, we find that the ratio of rotational support and thermal pressure is $v_{max} \sin(I)/\sigma = 0.47 - 3.21$ with a median of 2 ± 0.2 , which is slightly higher than other studies of star forming galaxies at a similar redshift (Daddi et al. 2010; Tacconi et al. 2011), though as our redshift range is more recent this could be seen as an indication of star forming galaxies having lower velocity dispersions at lower redshift. This ratio is much reduced from the $\sim 10-20$ observed in local spirals, indicating a higher gas fraction. At least 60 of our galaxies are found to have velocity fields consistent with having their ionised gas in a large ro-

tating disk. Of these, we detect a turnover in the rotation curve of 24. For galaxies with derivable rotation curves, we calculate the inclination corrected velocities. Galaxies with noticeable velocity gradients were classed as rotation dominated, galaxies without were classed as dispersion dominated. We find that dispersion dominated galaxies have a greater median stellar mass than the rotation dominated systems, in agreement with studies that suggest that lower stellar mass systems have higher gas fractions and negligible rotation (Förster-Schreiber et al. 2009; Law et al. 2009).

4) We find evidence for a clumpy morphology in our galaxies, though the realness of this is hard to determine without comparison images in the optical.

5) We calculate the specific angular momentum of our galaxies and find that they match well with the $j - M_\star$ relationship from Fall & Romanowski (2013), which suggests that this parameter space can be used as a physics based alternative to the Hubble tuning fork diagram in galaxy morphology classification. We find that the parameter space that our galaxies occupy is comparable with known S type galaxies, providing further evidence that our galaxies are rotating disks.

6) Using spatially resolved $H\alpha$ dynamical measurements, we calculate the value of the spin parameter λ_R for our galaxies and find a median of 0.55 ± 0.04 . We also find that λ_R has little relationship with stellar mass, agreeing with Burkett et al. (2015). The amount of scatter in $\lambda_R - M_\star$ compared to $j - M_\star$ suggests that λ_R 's usage as a proxy for j is limited.

7) Using the previously derived rotation curves for our galaxies, we use the virial theorem to calculate the dynamical masses of our galaxies. We find a median of $(7.9 \pm 4.5) \times 10^{10} M_\odot$ for the well-defined rotation curves. Assuming that dark matter constitutes 70% of each galaxy's mass, we calculate a median f_{gas} of 0.2 ± 0.1 . When we remove the galaxies which had

$f_{gas} < 0$, possibly caused by underestimations of the stellar mass, this value rises to 0.51 ± 0.06 . Both of these results are in good agreement with previous studies which find $f_{gas} = 0.2 - 0.8$ for star forming galaxies at high redshift (Daddi et al. 2010; Tacconi et al. 2010). These high gas fractions indicate that there are substantial gas reservoirs available to fuel star formation at this redshift.

In conclusion, we have demonstrated that integral field spectroscopy of the H α line emitted by high redshift galaxies can be used to prove that a large fraction of these star forming galaxies have large amounts of neutral hydrogen gas available to fuel star formation, and that their ionised gas is in large, rotating disks. Dynamical observations can be used to constrain the evolutionary models which are explored in numerical simulations.

Acknowledgements

I would like to thank my project supervisor Mark Swinbank, who guided me through this project and made himself available at any time, day or night, to answer my many questions.

6 References

- Asplund M., Grevesse N., et al., 2004, ApJ, 417, 751
 Bastian, N., Covey, K. R., Meyer, M. R., 2010, ARA&A, 48, 339–389
 Bell E. F., et al. 2005, ApJ, 625, 23
 Bournaud F., Elmegreen B. G., 2009, ApJ, 694, L158
 Bromm V., Kudritzki R. P., Loeb A., 2001, ApJ, 552, 464
 Bruzual G., Charlot S., 2003, MNRAS, 344, 1000
 Calzetti D., Armus L., et al. 2000, ApJ, 533, 687
 Cappellari M., Emsellem E., et al., 2011, MNRAS, 413, 813
 Charlot S., Fall S. M., 2000, ApJ, 539, 718
 Courteau S., 1997, AJ, 114, 2402
 Crain R. A., Theuns T., et al., 2009, MNRAS, 399, 1773
 Daddi E. et al., 2010, ApJ, 713, 686
 Darg D. W., Kaviraj S., et al., 2010, MNRAS, 401, 1043
 Davies R. I., et al. 2013, AA, 558, A56
 Dekel A. et al., 2009, Nat, 457, 451
 Dekel A., Sari R., Ceverino D., 2009, ApJ, 703:785–801
 Dickinson M., Papovich C., Ferguson H. C., Budavari T. 2003, ApJ, 587, 25
 Di Matteo T., Springel V., Hernquist L., 2005, Nat, 433, 604
 Drory N., Bender R., Feulner G., Hopp, U., Maraston C., Snigula J., Hill G. J. 2004, ApJ, 608, 742
 Drory N., Salvato M., Gabasch A., Bender, R., Hopp U., Feulner G., Pannella M., 2005, ApJ, 619, L131
 Elmegreen, D.M., Elmegreen, B.G., Ravindranath, S., Coe, D., 2007, ApJ, 658, 763
 Emsellem E., et al., 2011, MNRAS, 414, 888
 Erb D. K., Steidel C. C., Shapley A. E., Pettini M., Reddy N. A., Adelberger K. L., 2006, ApJ, 647, 128
 Fontana A., et al. 2003, ApJ, 594, L9
 Förster-Schreiber N. M., et al. 2009, ApJ, 706, 1364
 Feulner G., et al., 2005, ApJ, 633, L9
 Fogarty K., Postman M., Connor T., et al., 2015, ApJ, 813, 117
 Fontana A., et al. 2004, A&A, 424, 23
 Gabor J. M., Davé, R., Finlator K., Oppenheimer B. D., 2010, MNRAS, 407, 771
 Geach J. E., Smail I., Moran S. M., MacArthur L. A., Lagos C. d. P., Edge A. C. 2011, ApJ, 730, L19
 Genzel, R., et al. 2008, ApJ, 687, 59
 Genzel R., Tacconi L. J., et al. 2010. MNRAS 407, 2091
 Genzel R., Newman S., Jones T., Förster Schreiber N. M., Shapiro K., et al. 2011, ApJ, 733, 101
 Hall M., Courteau S., Dutton A.A., McDonald M., Zhu Y., 2012, MNRAS, 425, 2741
 Hammer F., Flores H., Elbaz D., Zheng X. Z., Liang Y. C., Cesarsky C., 2005, A&A, 430, 115
 Hogg D. W., 2000, preprint (astro-ph/9905116)
 Hollas M.J., Modern Spectroscopy (3rd ed.). (1996), Wiley. pp. 30–34. ISBN 0471965227.
 Holmberg E., 1946, Lund Medd, Ser. II, No. 117
 Kennicutt R. C., 1998, ARA&A, 36, 189
 Kereš D., Katz N., Wineberg D. H., Davé R., 2005, MNRAS, 327
 Kereš D., Katz N., et al., 2009, MNRAS, 396, 2332
 Kewley L. J., Dopita M. A., 2002, ApJ, 142, 35
 Koekemoer A. M., et al., 2007, ApJ, 172, 196
 Kunth D., Östlin G., 2000, AAR, 10, 1
 Law D. R., Steidel C. C., Erb J. E., et al. 2009, ApJ, 697, 2057
 Lehnert M. D., Nesvadba N. P. H., Tiran L. L., Matteo P. D., van Driel W., et al. 2009, ApJ, 699, 1660
 Madau P., Dickinson M., 2014, ARA&A, 52
 McCarthy I. G., Schaye J., Font A. S., et al., 2012, MNRAS, preprint (arXiv:1204.5195)
 Navarro J. F., Steinmetz M., 2000, ApJ, 538, 477
 Pettini, M., Pagel, B. E. J., 2004, MNRAS, 348, 59
 Prantzos N., 1998, ASP Conf. Ser. 141, 171
 Querejeta M., et al. 2015, ApJs, 219, 5
 Quyrel J., et al., 2012, A&A, 539, A93
 Romanowsky A. J., Fall S. M., 2012, ApJS, 203, 17
 Romanowsky A. J., Fall S. M., 2013, ApJ, 769, L26
 Salpeter E., 1955, ApJ, 121, 161
 Shapley AE., 2011, ARI, 9:36
 Sharples R. et al., 2013, The Messenger, 151, 21
 Snow T. P., Witt A. N., 1996, ApJ, 654, L33
 Sobral D., et al. 2012, MNRAS, preprint (arXiv:1202.3436)
 Solway M., Sellwood J. A., Schönrich R., 2012, MNRAS, 422, 1363
 Swinbank A. M. et al. 2010, MNRAS, 405, 234
 Swinbank A. M. et al. 2011, ApJ, 742, 11
 Swinbank A. M., Sobral D., Smail I., Geach J. E., Best P. N., McCarthy I. G., Crain R. A., Theuns T., 2012, MNRAS, 426, 935
 Tacconi L. J. et al., 2010, Nat, 463, 781
 Tinsley B. M., 1968, ApJ, 674, 29
 Tonini C., Lapi A., Salucci P., 2006 ApJ, 649, 591
 Torres-Peimbert S., Peimbert M., Fierro J., 1989, ApJ, 345, 186
 van de Voort F., Schaye J., Booth C. M., Haas M. R., Dalla Vecchia C., 2011 MNRAS, 414, 811
 van de Voort F., Schaye J., Altay G., Theuns T., 2012, MNRAS, 421, 2809
 Yoshikawa T., Akiyama M., et al., 2010, ApJ, 718, 112
 Young J. S., Scoville N. Z., 1991, ARA&A, 29, 581
 Yuan T.-T., Kewley L. J., et al., 2011, ApJ, 732, L14
 Yuan T.-T., Kewley L. J., et al., 2013, ApJ, 763, 9

7 Appendix

In this Appendix we present additional material to the main report. These include the full set of derived maps, and images which, while are not strictly necessary, can aid in the reader's understanding of the content covered.²

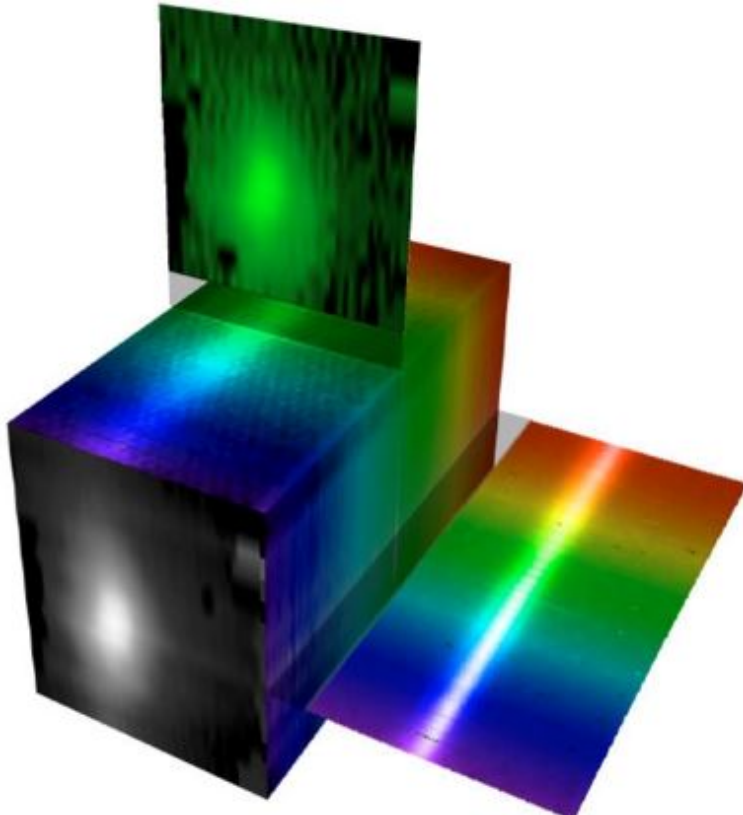


Figure 22: An artistic impression of a data cube. The 3D array is composed of two spatial axes and one of wavelength, allowing for the analysis of integrated and spatially resolved galaxy properties by the construction of an emission spectrum for a chosen group of pixels in the spatial axes. Fixing these pixels, we measured how the observed flux changed with wavelength to construct this spectrum.

²Data cube image is taken from lsit-miv.u-strasbg.fr/paseo/cubevisualization.php.

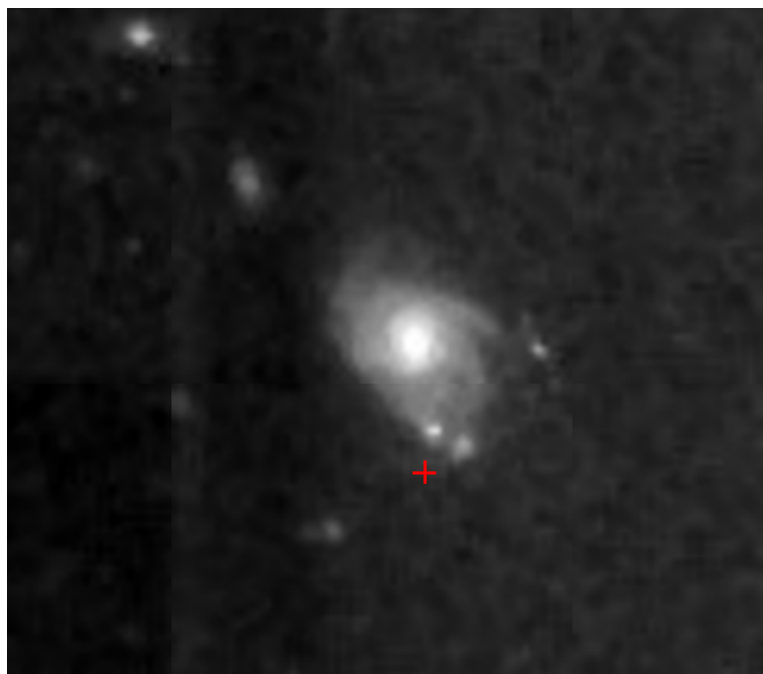


Figure 23: Optical image of a high-redshift star forming galaxy taken by the Hubble Space Telescope. Observable is a clumpy morphology, which we believe to see in our $H\alpha$ derived dynamical fields. Comparing optical and $H\alpha$ images could allow us to comment on the realness of the clumps that we believe to be able to see beyond the main star forming bodies of our galaxies.

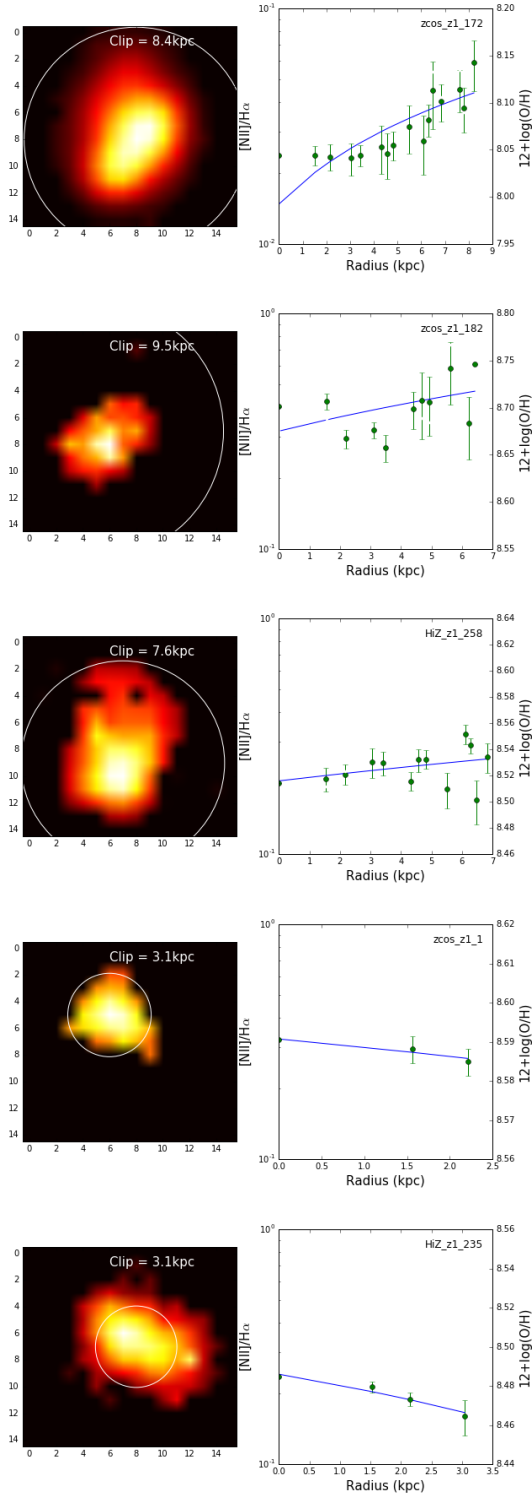
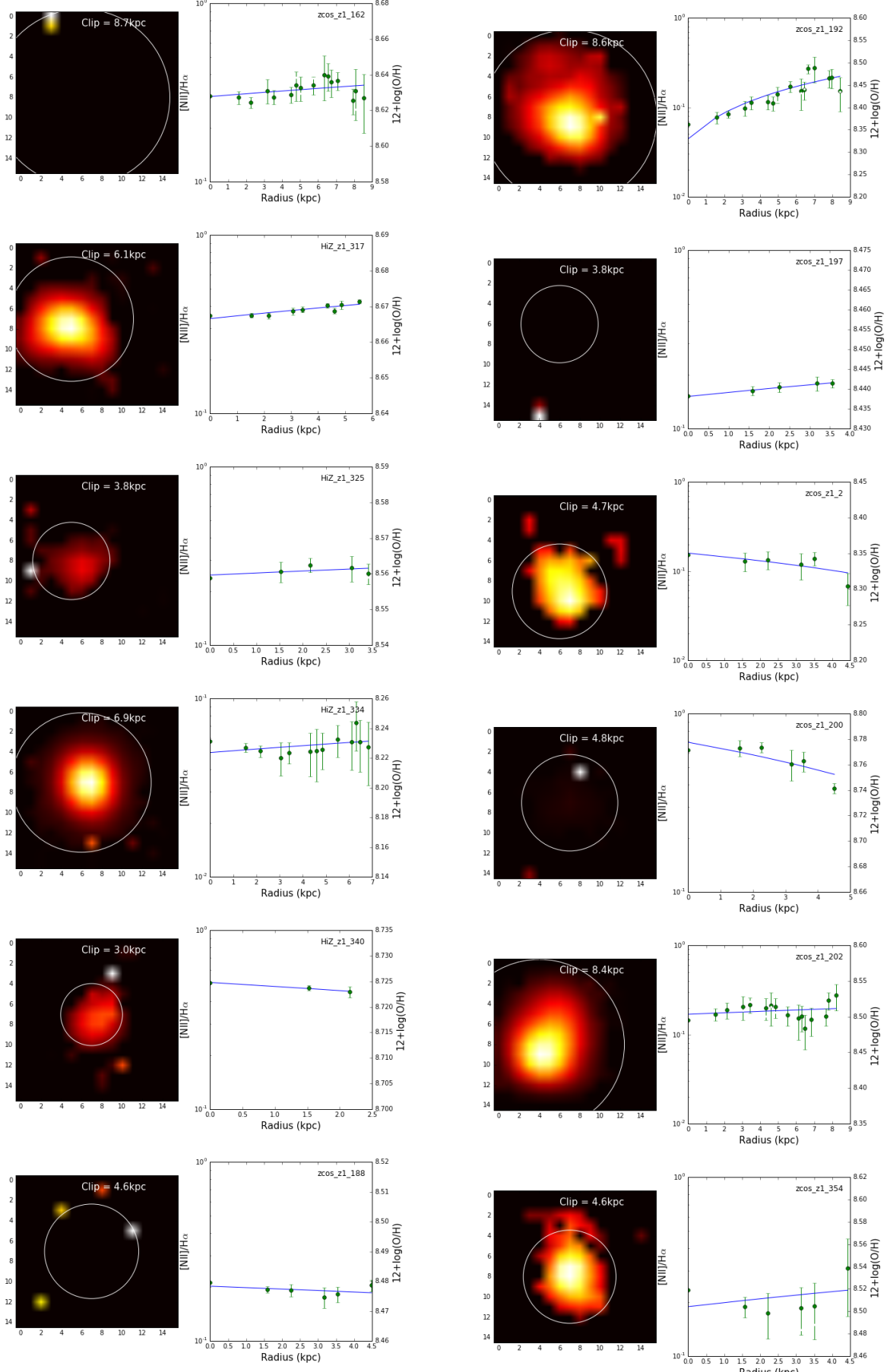
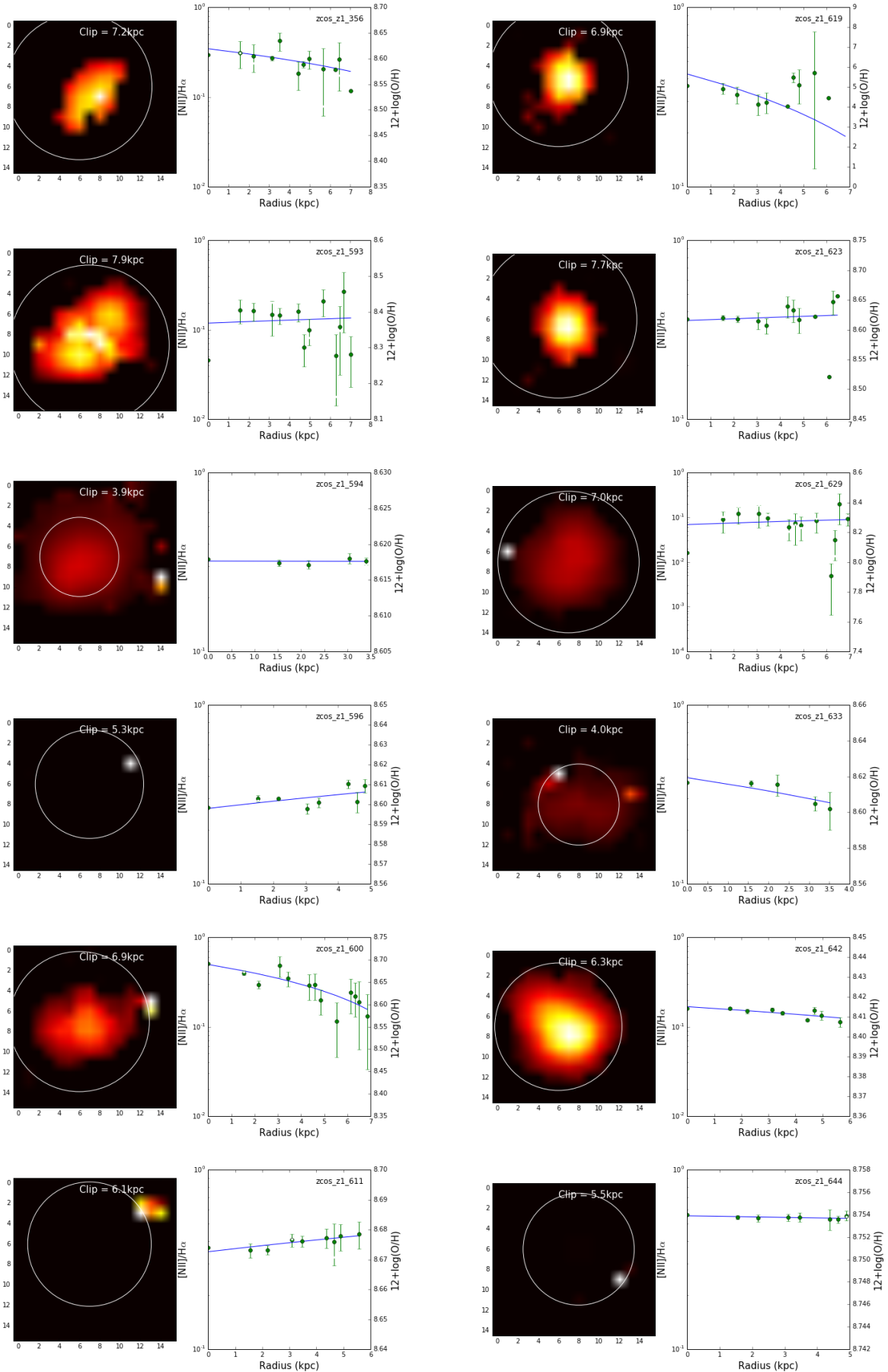
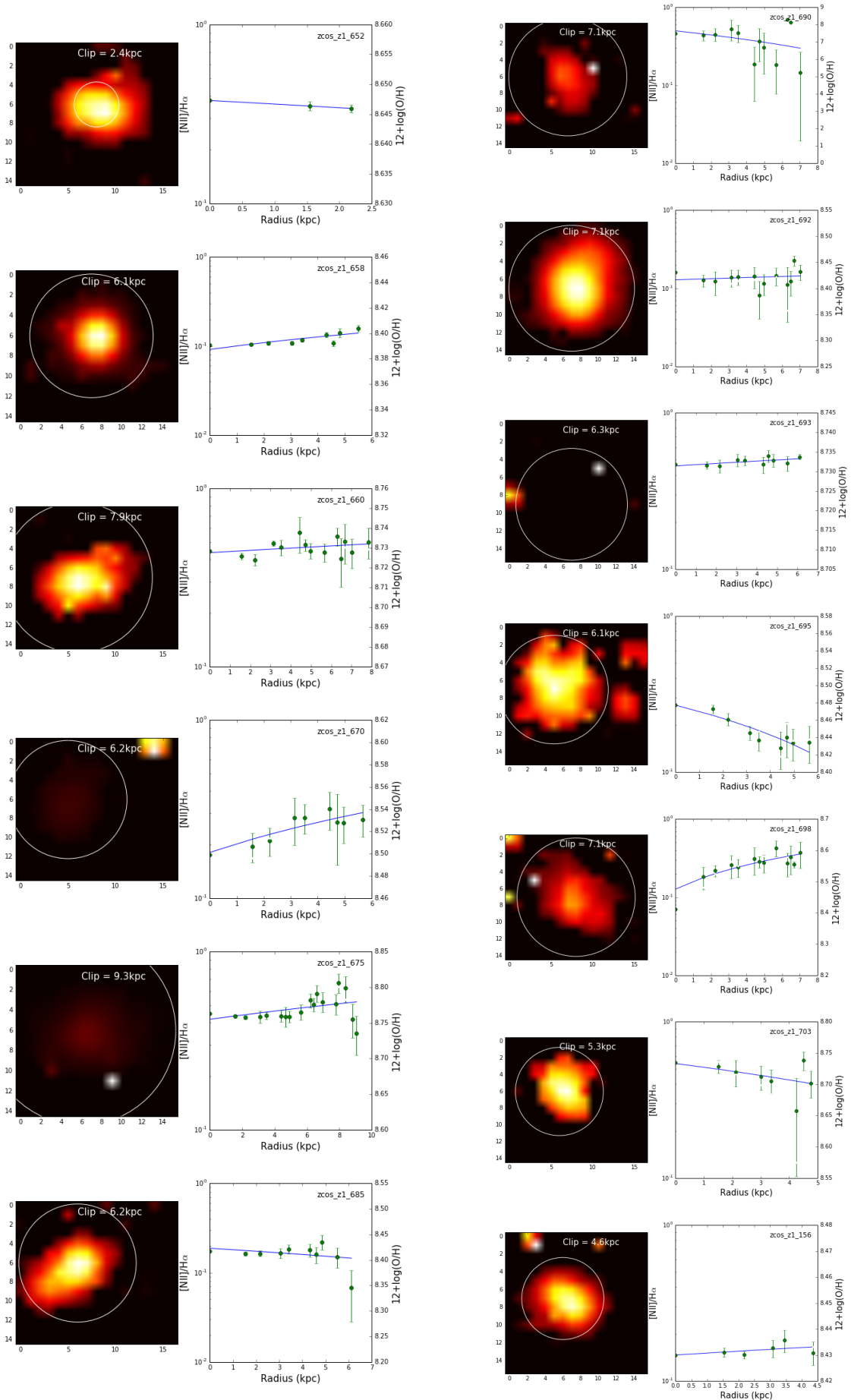


Figure 24: Metallicity gradients for the 55 galaxies for which spatially resolved measurements could be made. (**Left**) H α flux maps. The solid white circle represents the area from which the [NII]/H α ratios were extracted, the radius being determined by the maximum observed radius during our measurement of a 1D integrated rotation curve in Section 4.1. (**Right**) The ratio [NII] $\lambda 6583$ /H α plotted against the physical radius. The blue line represents the linear line of best fit. Only half of the gradients were negative, as would be expected for growth starting at the bulge and working outwards. Positive gradients could be accounted for by the effects of inclination.







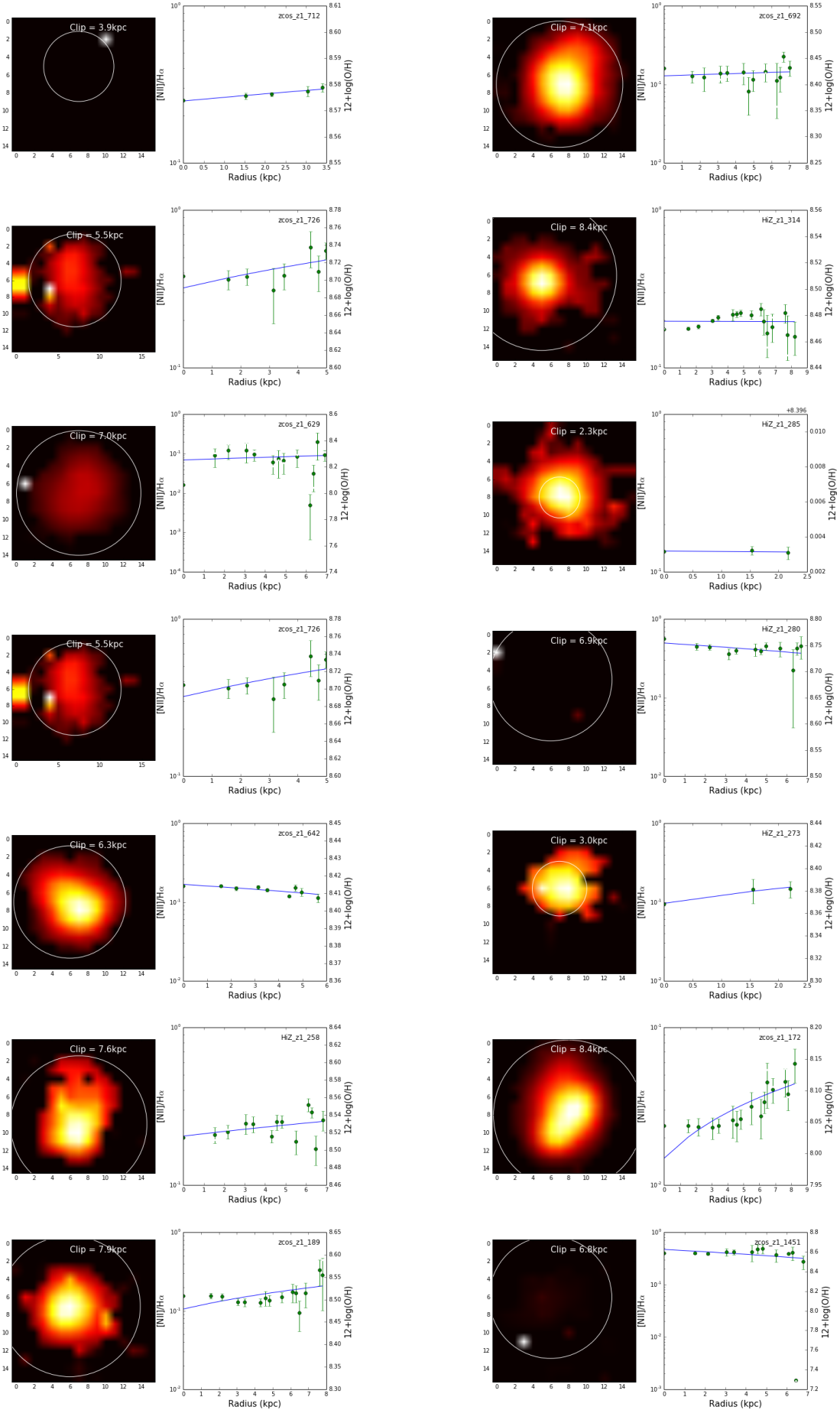


Figure 25: (Left to right) Raw H α narrowband image, H α flux field, two dimensional velocity field, velocity dispersion field and integrated one dimensional rotation curve. The black marker in the rotation curve represents $\pm 20\text{km}\text{s}^{-1}$. The error bars in the curve have been removed to improve clarity.

